

# Characterization of the lid-driven cavity magnetohydrodynamic flow at finite magnetic Reynolds numbers using far-field magnetic boundary conditions

Charles Kawczynski, Sergey Smolentsev, and Mohamed Abdou

Citation: [Physics of Fluids](#) **30**, 067103 (2018); doi: 10.1063/1.5036775

View online: <https://doi.org/10.1063/1.5036775>

View Table of Contents: <http://aip.scitation.org/toc/phf/30/6>

Published by the [American Institute of Physics](#)

---

## Articles you may be interested in

[The effect of surface roughness on rotor-stator cavity flows](#)

[Physics of Fluids](#) **30**, 064103 (2018); 10.1063/1.5028209

[Spectra and Mach number scaling in compressible homogeneous shear turbulence](#)

[Physics of Fluids](#) **30**, 065109 (2018); 10.1063/1.5028294

[Buoyancy induced turbulence modulation in pipe flow at supercritical pressure under cooling conditions](#)

[Physics of Fluids](#) **30**, 065105 (2018); 10.1063/1.5029892

[Effect of gap flow on the shallow wake of a sharp-edged bluff body—Coherent structures](#)

[Physics of Fluids](#) **30**, 065107 (2018); 10.1063/1.5022252

[Direct numerical simulation of quasi-equilibrium turbulent puffs in pipe flow](#)

[Physics of Fluids](#) **30**, 064102 (2018); 10.1063/1.5031884

[Bubble dynamics and atomization mechanisms in burning multi-component droplets](#)

[Physics of Fluids](#) **30**, 067101 (2018); 10.1063/1.5035384

---

PHYSICS TODAY

WHITEPAPERS

### ADVANCED LIGHT CURE ADHESIVES

Take a closer look at what these environmentally friendly adhesive systems can do

READ NOW

PRESENTED BY  
 MASTERBOND  
ADHESIVES | SEALANTS | COATINGS

# Characterization of the lid-driven cavity magnetohydrodynamic flow at finite magnetic Reynolds numbers using far-field magnetic boundary conditions

Charles Kawczynski, Sergey Smolentsev,<sup>a)</sup> and Mohamed Abdou  
 UCLA, MAE Department, 44-114 Engineering IV, 420 Westwood Plaza, Los Angeles,  
 California 90095-1597, USA

(Received 18 April 2018; accepted 5 June 2018; published online 25 June 2018)

The lid-driven cavity (LDC) flow is a canonic hydrodynamic problem. Here, a 3D LDC flow of electrically conducting, incompressible fluid is studied numerically in the presence of a strong magnetic field, which is applied parallel to the lid plane and perpendicular to the direction of the lid motion. The cavity has electrically conducting walls of finite thickness and an infinitely thin moving lid. The problem is characterized by three dimensionless parameters: the Reynolds number ( $Re$ ), the Hartmann number ( $Ha$ ), and the magnetic Reynolds number ( $Re_m$ ). The primary research focus is on the effect of  $Re_m$ , which was changed in the study from  $Re_m \ll 1$  to the maximal  $Re_m = 2000$  at which dynamo action may be expected, while  $Ha = 100$  and  $Re = 2000$ . The computational approach is based on the utilization of far-field magnetic boundary conditions by solving the full magnetohydrodynamic (MHD) flow problem at finite  $Re_m$  for a multi-material domain composed of the inner conducting liquid, conducting walls, and sufficiently large insulating outer domain called “vacuum” (the induced magnetic field vanishes at the vacuum boundaries) using a fractional-step method. The computed results show many interesting features with regard to the effect of  $Re_m$  on the MHD boundary layer and the bulk flow, generation of a magnetic field and its penetration into vacuum, energy balance, tendency of the magnetic field to become frozen in the fluid and associated magnetic flux expulsion, transition to unsteady flows, and self-excitation of the magnetic field and the associated dynamo-type action at high  $Re_m$ . Published by AIP Publishing. <https://doi.org/10.1063/1.5036775>

## I. INTRODUCTION

Electrically conducting liquids such as liquid metals (LMs), molten salts, and electrolytes, when moving in a domain of dimension  $L$  with the velocity  $V$  in the presence of an externally applied magnetic field ( $\mathbf{B}^0$ ), induce an additional magnetic field ( $\mathbf{B}^1$ ). The induced electric currents ( $\mathbf{j}$ ) associated with the induced magnetic field interact with the total magnetic field ( $\mathbf{B} = \mathbf{B}^0 + \mathbf{B}^1$ ), giving rise to an electromagnetic (EM) Lorentz force ( $\mathbf{f}_L = \mathbf{j} \times \mathbf{B}$ ). This EM force can become appreciable and impact the flow in many ways. Such flows are termed magnetohydrodynamic (MHD) flows and exist in nature (e.g., astrophysical and geophysical flows) and engineering applications (e.g., plasma confinement, LM cooling in fusion reactors, and EM casting). Magnetohydrodynamic flows are often categorized by the measure of the ratio of magnetic field convection to diffusion. A dimensionless parameter, the magnetic Reynolds number ( $Re_m = VL/\nu_m$ ), is typically used as an estimate for this measure. Here,  $\nu_m = (\sigma_l^{-1}\mu_m^{-1})$  is the magnetic viscosity, the inverse product of liquid electrical conductivity ( $\sigma_l$ ) and magnetic permeability ( $\mu_m$ ). The magnetic Reynolds number appears in the magnetic induction equation when transformed into a dimensionless form by using appropriate scales. Low and high  $Re_m$  MHD flows have been studied for years (see, e.g., Refs. 1–7). In astrophysical MHD

flows, the  $Re_m$  is very high (typically  $Re_m \sim 10^{10}$ – $10^{20}$ , Ref. 1), resulting in a convection-dominated regime where magnetic field lines are frozen into the fluid and have to move along with it. By contrast, the  $Re_m$  is typically small ( $Re_m \ll 1$ ) in LM applications because the product of the velocity and length is small compared to the magnetic viscosity. In such diffusion-dominated regimes, the  $Re_m$  acts as a ratio between the induced and applied magnetic fields. Assuming  $|\mathbf{B}^1| \ll |\mathbf{B}^0|$  allows for the so-called “inductionless approximation” (also known as a low  $Re_m$  or quasi-static approximation), where the mathematical complexity of the MHD problem is significantly reduced by the use of a scalar field—electric potential ( $\phi$ )—as the main EM variable.

Although it is widely believed that all LM applications exhibit  $Re_m \ll 1$ , there are a few important cases where  $Re_m$  is of the order of unity or even higher. As demonstrated in the recent past, the helical flow inside one of the MHD pumps of the fast breeder reactor Superphenix in France (see Ref. 8) exhibited a  $Re_m$  of 25, suggesting a possibility of the dynamo regime, when self-excitation of a magnetic field occurs. Achieving sufficiently high  $Re_m$  in the range  $10^1$ – $10^3$  has been the goal of many dynamo experiments (see Molokov *et al.*, Dynamo Experiments in Ref. 9) tending to elucidate the origin of the planetary magnetic fields. A flow in a blanket of a fusion power reactor, where pure lithium or lithium-containing alloy circulates slowly for power conversion and tritium breeding in the presence of a strong plasma-confining

<sup>a)</sup>Electronic mail: sergey@fusion.ucla.edu

magnetic field, is another example of MHD flows where  $Re_m > 1$  might be possible. Such a flow is likely to happen in the abnormal conditions of a plasma disruption when the poloidal component of the plasma-confining magnetic field suddenly drops from its nominal value [1 (T)] to zero at the time scale of milliseconds (see Ref. 10). This most extreme and unsteady event in the fusion plasma can cause high-velocity flows in the LM of the order of 10 (m/s), resulting in a  $Re_m$  of 5-10. These magnitudes of  $Re_m$  look insufficient to cause any dynamo action, but many interesting flow features can be expected that cannot be analyzed using the inductionless approximation.

A brief discussion on terminology is warranted. We define the word “finite” as a fixed amount that is not infinitely small and not infinitely large. This definition indicates that convection and diffusion both contribute to the induction equation for finite  $Re_m$  MHD flows.

When characterizing the MHD flow physics at finite  $Re_m$ , we limited our considerations to the well-known ordinary hydrodynamic lid-driven cavity (LDC) flow problem for the following reasons. First, the 3D LDC flow configuration was widely studied under purely hydrodynamic conditions, is well understood, and thus can serve as a convenient “test-bed” in the case of MHD flows. Many anticipated flow features in the LDC flow problem are expected to be common to other wall-confined MHD flows like those in the blanket conduits or dynamo experiments. Second, many MHD flow configurations lead to relatively simple quasi-two-dimensional (Q2D) magnetic field solutions, especially in the case of rectangular ducts (Ref. 11). Third, the 3D LDC MHD flow may result in true 3D physics by making the three flow dimensions similar:  $L_x \sim L_y \sim L_z$ . Fourth, the associated computer code seems to be simpler and the computational time lesser compared to complex geometry flows, thus allowing for detailed studies of the effect of  $Re_m$  and other parameters on the flow. Numerical computations of a 3D LDC finite  $Re_m$  MHD flow were performed by Ref. 12; however, boundary conditions (BCs) in this study were inappropriately applied at the fluid domain boundary. Induced magnetic fields in conducting fluids are, in general, free to pass beyond the conducting fluid, solid material, and even into the vacuum. Hence, results in Ref. 12 for the LDC MHD flow may be unphysical and unsuited as a benchmark for experiments and numerical studies.

The three dimensionless parameters that define the LDC flow in a magnetic field are the hydrodynamic Reynolds number  $Re = \rho V L / \mu$ , the Hartmann number  $Ha = B^0 L \sqrt{\sigma_l / (\rho \nu)}$ , and the already mentioned magnetic Reynolds number  $Re_m$ . Here,  $B^0$ ,  $\rho$ ,  $\mu$ , and  $\nu$  are the characteristic magnetic field, density, and dynamic and kinematic viscosity of the fluid, respectively. The  $Re$  and  $Ha^2$  estimate the ratio of inertial to viscous forces and EM to viscous forces, respectively. While the effects of the Reynolds and Hartmann numbers are well understood (see, e.g., Refs. 13–15), the influence of  $Re_m$  has not been fully evaluated yet. That is why we focus here on LM MHD flows with finite  $Re_m$  values that are around or higher than unity but much smaller than those in the astrophysical applications. To clearly illustrate the effect of  $Re_m$ , we start with  $Re_m \ll 1$  and gradually increase it until the observed finite  $Re_m$  effects become pronounced, even dominating. In this way,

the maximal  $Re_m$  in this study was 2000 that exceeds those in all LM applications but is necessary from the theoretical and methodological viewpoints.

When the magnetic field is used as the primary EM variable, the magnetic BCs are another practical issue in constructing the computational model. Magnetic BCs are required to solve the magnetic induction equation but pose computational difficulties which, in the past, have been circumvented by making simplifying assumptions. The most physically reliable and widely applicable magnetic BC treatment is to assert that the induced magnetic field generated in the liquid penetrates into surrounding vacuum and diffuses to zero at infinity. However, this is difficult to enforce in practice. These far-field magnetic BCs are referred to here as real-vacuum (RV) BCs. Due to the challenges associated with RV BCs, approximate local magnetic BCs have been developed to circumvent the formidable challenges associated with enforcing RV BCs. One of the most popularly used approximate magnetic BCs is commonly called pseudo-vacuum (PV) BCs. A wide range of MHD flows have been successfully described using PV BCs (see, e.g., Refs. 16–18). The PV BCs force magnetic field lines perpendicular to the conductor boundary and are accurate when  $Re_m \ll 1$ , i.e., when the inductionless approximation holds (see Ref. 17). It is noteworthy that PV BCs are a particular case of ensuring magnetic field continuity at the boundary. In this study, we abandon the approximate PV BCs in favor of RV BCs as the  $Re_m$  in the present study is much higher than unity. There are also difficulties associated with implementing RV BCs when solving the induction equation continuously across the large-sized multi-material domain including discontinuities in the electrical conductivity.

In the present study, the incompressible MHD equations for finite  $Re_m$  are solved numerically to simulate a 3D LDC flow between  $Re_m \ll 1$  and  $Re_m = 2000$ . A large external vacuum domain surrounds the conducting fluid and walls to enforce physically accurate far-field magnetic field BCs. Velocity, electric current and magnetic field distributions, and energy balance components are analyzed. Along with deeper insight into the flow physics, we hope to establish in this paper a reliable benchmark for future finite  $Re_m$  studies. The paper is organized as follows. Sections II–V present our mathematical formulation, numerical methodology, results and discussion, and conclusions, respectively.

## II. PROBLEM FORMULATION

### A. Governing equations

For the reference MHD LDC flow problem, consider a total domain ( $\Omega_t$ ) composed of a conducting fluid ( $\Omega_f$ ), conducting solid wall ( $\Omega_w$ ), and vacuum ( $\Omega_v$ ) domain. Let  $\Omega_c$  denote the conducting domain and  $\Gamma_f$ ,  $\Gamma_c$ ,  $\Gamma_t$ , and  $\Gamma_{lid}$  denote the boundaries of the fluid, conductor, total, and driving lid, respectively (Fig. 1).

Using half of the cavity width in the applied magnetic field direction  $L$ , velocity  $U$ , time  $L/U$ , pressure  $\rho U^2$ , magnetic field  $B^0$ , and electric current density  $\sigma_l U B^0$  as the scales, the incompressible and isothermal momentum, induction, mass continuity, and magnetic field continuity equations for

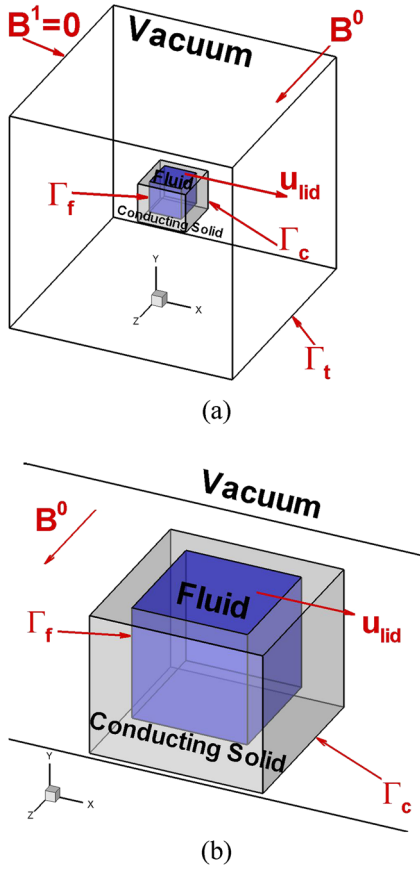


FIG. 1. (a) Schematic for the LDC MHD flow problem using RV BCs. (b) Zoomed view.

uniform material properties (except electrical conductivity) can be written in the dimensionless form,

$$\frac{\partial \mathbf{u}}{\partial t} + (\mathbf{u} \cdot \nabla) \mathbf{u} + \nabla p = \frac{1}{Re} \nabla^2 \mathbf{u} + \frac{Ha^2}{Re} \mathbf{j} \times \mathbf{B}, \quad \text{in } \Omega_f, \quad (1)$$

$$\mathbf{j} = \frac{1}{Re_m} \nabla \times \mathbf{B}, \quad \text{in } \Omega_c, \quad (2)$$

$$\frac{\partial \mathbf{B}}{\partial t} + Re_m^{-1} \nabla \times \left( \frac{1}{\bar{\sigma}} \nabla \times \mathbf{B} \right) = \nabla \times \mathbf{u} \times \mathbf{B}, \quad \text{in } \Omega_r, \quad (3)$$

$$\nabla \cdot \mathbf{u} = 0, \quad \text{in } \Omega_f, \quad (4)$$

$$\nabla \cdot \mathbf{B} = 0, \quad \text{in } \Omega_r. \quad (5)$$

Here,  $\mathbf{u}$ ,  $p$ ,  $\mathbf{j}$ , and  $\mathbf{B} = \mathbf{B}^0 + \mathbf{B}^1$  are velocity, pressure, electric current density, and the total magnetic field, composed of the applied plus induced field, respectively. In addition to  $Re$ ,  $Ha$ , and  $Re_m$ , the normalized electrical conductivity ( $\bar{\sigma} = \sigma/\sigma_l$ ) is defined as the local electrical conductivity ( $\sigma$ ) divided by the liquid electrical conductivity.

Equations (4) and (5) are divergence-free constraints that ensure  $\mathbf{u}$  and  $\mathbf{B}$  remain solenoidal, respectively. There is no guarantee that Eq. (5) will be satisfied when integrating Eq. (3), especially over long periods, which may lead to unphysical forces in the momentum equation (Refs. 19–21). Several methods can be used to enforce Eq. (5) and will be discussed in Sec. III.

Equation (3) is valid everywhere in space, but inspecting how it simplifies in the vacuum is insightful. In the vacuum, Eq. (3) can be written in the following form:

$$\nabla \times (\nabla \times \mathbf{B}) = \mathbf{0}, \quad \text{in } \Omega_v. \quad (6)$$

The convection term has vanished because  $\mathbf{u} = \mathbf{0}$ , and the unsteady term has vanished because  $\sigma = 0$ , resulting in the absence of  $Re_m$ . The absence of the unsteady term implies that the magnetic field travels infinitely fast in the vacuum domain. This equation may be cast into the form of a Poisson equation, which is more convenient for solving, using the vector identity  $\nabla \times (\nabla \times \mathbf{B}) = \nabla (\nabla \cdot \mathbf{B}) - \nabla^2 \mathbf{B}$  and the divergence-free constraint such that

$$\nabla^2 \mathbf{B} = \mathbf{0}, \quad \text{in } \Omega_v. \quad (7)$$

While there are no electric currents in the vacuum, the magnetic field permeates into the vacuum, and its strength decreases with distance from the conductor. Providing that the electric current is known, the magnetic field at any point in space can be computed using the Biot-Savart law (Ref. 22). The Biot-Savart law can be written, using the scales defined in this study, as

$$\mathbf{B}(\mathbf{x}) = \frac{Re_m}{4\pi} \int_{\Omega_c} \mathbf{j}(\mathbf{x}') \times \frac{\mathbf{r}}{|\mathbf{r}|^3} d^3 \mathbf{x}', \quad \mathbf{r} = \mathbf{x} - \mathbf{x}'. \quad (8)$$

Here,  $\mathbf{x}$ ,  $\mathbf{x}'$ , and  $\mathbf{r}$  are the dimensionless spatial coordinate vector, dummy variable for integration, and distance vector from  $\mathbf{x}$  to  $\mathbf{x}'$ , respectively. According to Eq. (8), the magnetic field strength decreases with  $1/|\mathbf{r}|^3$  in the vacuum domain. This decay rate is a useful result to help determine the size of a sufficiently large vacuum domain such that the induced magnetic field approximately satisfies  $\mathbf{B}^1 = \mathbf{0}$  at  $\Gamma_t$  naturally.

## B. Velocity and pressure boundary conditions

Equations (1)–(3) require BCs. For velocity, the no-slip condition was used on  $\Gamma_f$ . For a LDC flow, this simplifies to a tangential velocity component of unity at the driving lid, and zero velocity elsewhere. The pressure Poisson equation, derived by taking the divergence of Eq. (1), requires BCs for pressure. Pressure BCs can be determined directly from Eq. (1). For pressure, we used the commonly applied BCs,  $(\mathbf{n} \cdot \nabla)p = 0$  on  $\Gamma_f$  (see Ref. 23). Here,  $\mathbf{n}$  is the outward surface normal unit vector.

## C. Magnetic boundary conditions

The RV magnetic BCs are mathematically expressed as

$$\mathbf{B} = \mathbf{0}, \quad \text{at } \Gamma_t \rightarrow \infty. \quad (9)$$

To simulate MHD flows using directly RV BCs in general geometric domains requires special care and is a formidable task because the magnetic field can pass the conductor boundary and penetrate deep into the vacuum, where its transport is infinitely fast. This infinitely fast transport of the magnetic field in vacuum results in a non-trivial distribution and the inability to apply point-wise (local) magnetic BCs at the conductor boundary. Several tactics have been used over the years to enforce RV BCs for general geometries. Some are discussed here.

The first method is to formulate special magnetic BCs on the conductor boundary, when the magnetic field in the vacuum is of no interest, and solve the mathematical equations governing the BCs (see Refs. 24 and 25). The boundary-element method (BEM) can be applied to enforce these special magnetic RV BCs. This approach is elegant and does not require extending the computational domain; however, it requires the solution of a dense and non-symmetric partial integro-differential equation on the conductor boundary.

The second and third methods involve surrounding the conducting region (fluid and solid) with an electrically insulating exterior and set the magnetic field to zero at a finite distance sufficiently far from the conductor such that the solution in the conductor is no longer affected. Reference 26 found that errors associated with truncating the vacuum domain to a finite distance were reduced to less than 0.5% for an insulating domain five times larger than the conducting domain. Equations are then solved separately (method two) and then iteratively matched between the conductor-insulator interface or continuously (method three) across a domain of variable electrical conductivity. Method three is used in the present paper.

In the cases presented for  $Re_m \ll 1$ , PV magnetic BCs are used, and the exterior vacuum domain is not needed. Pseudo-vacuum magnetic BCs are mathematically expressed as

$$(\mathbf{n} \cdot \nabla)(\mathbf{B} \cdot \mathbf{n}) = 0, \quad (\mathbf{B} \times \mathbf{n}) = \mathbf{0}, \quad \text{on } \Gamma_c. \quad (10)$$

Equation (10) is applied at the conductor boundary and enforces electric currents tangent to the boundary surface. These BCs are a valid approximation to RV BCs in the low  $Re_m$  limit but do not hold true for arbitrary  $Re_m$  (Ref. 17).

#### D. The computational domain configuration and parameter space

In the present paper, we consider a lid-driven square cavity MHD flow with a transversely applied magnetic field as shown in Fig. 1. This flow is an internal circulating one, driven by the shear stress at the top lid. Momentum is diffused and advected downstream of the lid and eventually re-circulates back to the top of the cavity.

The lid-driven cavity flow is a classic hydrodynamic flow configuration and was used in an enormous number of studies. This flow configuration has been extensively studied for purely hydrodynamic flows (see, e.g., Refs. 13, 27, and 28), where  $Re$  is the only dimensionless parameter. The low  $Re_m$  MHD flow configuration has been studied fairly well (see, e.g., Refs. 12, 14, and 15) but much less than the purely hydrodynamic case. Part of this reason is that the parameter space increases significantly. In addition to  $Re$ ,  $Ha$  enters the momentum equation and the wall conductance ratio,  $c_w = \sigma_w t_w / (\sigma_l L)$ , enters the problem in the case of a thin conducting wall. Here,  $t_w$  and  $\sigma_w$  are the wall thickness and wall electrical conductivity, respectively. Furthermore, the orientation and distribution of the applied magnetic field are additional parameters that significantly affect the solution. Allowing for finite  $Re_m$  increases the solution space further. Also, this introduces some technical challenges on implementation of far-field magnetic BCs as discussed above.

General changes in physical flow features due to changes in these parameters are well known. Increasing  $Re$  thins the momentum boundary layer (BL) (where viscous forces dominate), increases the hydrodynamic flow development time, and pushes the flow toward an unsteady (increased further still) and turbulent regime. Increasing  $Ha$  thins the Hartmann BL (where EM and viscous forces balance), increases the EM force on the flow, which increases flow damping along the applied magnetic field direction, and decreases the flow development time. Increasing  $Re_m$  thins the magnetic BL (where the majority of the electric current is located, see Ref. 1), increases the ratio of convection to diffusion of the magnetic field, and increases the flow development time (see Ref. 29).

The conducting fluid is surrounded by a finite solid conducting wall on all sides of the cavity except the driving lid, which is infinitely thin (i.e., an interface). The vacuum domain extends beyond the fluid and wall domains [Fig. 1(a), a zoomed view in Fig. 1(b)] for arbitrary  $Re_m$ , and RV BCs are applied at the outer vacuum boundary. We consider a normalized cavity wall thickness ( $\bar{t}_w = t_w/L$ ) and normalized wall electrical conductivity ( $\bar{\sigma}_w = \sigma/\sigma_w$ ) of  $\bar{t}_w = 0.05$  and  $\bar{\sigma}_w = 1$ , respectively. Therefore, the wall conductance ratio is  $c_w = 0.05$ . A total domain roughly 7 times larger than the conducting domain by volume is used:  $\Omega_t = \{-7 \leq x, y, z \leq 7\}$ ,  $\Omega_f = \{-1 \leq x, y, z \leq 1\}$ , and  $\Omega_c = \{-(1 + \bar{t}_w) \leq x, z \leq (1 + \bar{t}_w), -(1 + \bar{t}_w) \leq y \leq 1\}$ . Initial conditions are  $\mathbf{u} = \mathbf{0}$  and  $\mathbf{B}^1 = \mathbf{0}$ . Velocity BCs are  $\mathbf{u} = (1, 0, 0)$  at  $y = 1$  and  $\mathbf{u} = \mathbf{0}$  elsewhere on  $\Gamma_f$ . Equation (10) is used when  $Re_m \ll 1$ , and Eq. (9) is used otherwise for the induced magnetic field BCs.

The externally applied magnetic field is in the  $z$  direction, parallel to the driving lid and perpendicular to the lid motion, to assist a steady flow regime. The other two applied field directions, along the  $x$  and  $y$  axes, may result in unstable flows (Refs. 12 and 15). All computations were performed at  $Re = 2000$ ,  $Ha = 100$ , and  $c_w = 0.05$ . The  $Re_m$  values considered were 0, 1, 100, 200, . . . , 1000, 1500, and 2000.

Given this flow configuration, the number, location, and flow intensity of recirculation zones depend on the dimensionless parameters. Also, due to  $\mathbf{B}^0$  aligned along the  $z$  direction, the flow is expected to be nearly uniform along the  $z$  direction due to suppression of motion along the magnetic field lines (Hartmann damping), at least for low and possibly moderate  $Re_m$ .

The flow is also expected to be symmetric with respect to  $u$ ,  $v$ ,  $p$ , and  $B_z$  and antisymmetric with respect to  $w$ ,  $B_x$ , and  $B_y$  at the  $z = 0$  plane. This symmetry and antisymmetry conditions were taken advantage of to reduce the computational domain by half. Additional calculations were performed in a fully 3D geometry with neither symmetry nor anti-symmetry BCs at  $Re_m = 1000$ , 1500, and 2000. Results confirmed that these symmetry and antisymmetry BCs are valid in the considered parameter range except for the two highest  $Re_m$  value cases, which are discussed in Sec. IV.

The chosen parameter space was selected very carefully. Reynolds number was chosen large enough such that inertial effects are not negligible. The Hartmann number was chosen large enough to let the flow exhibit distinctive Hartmann layers, but low enough not to cause extra computational challenges associated with the need for fine resolution of the thin BLs.

The  $Re_m$  was chosen from 0 to sufficiently large (but still moderate compared to astrophysical MHD flows) to see how the magnetic field convection-dominated regime, and potentially dynamo physics, begins.

We observed that the purely hydrodynamic flow is unsteady in the absence of the applied magnetic field but becomes steady in the presence of the applied magnetic field for almost all  $Re_m$  except for  $Re_m = 1500$  and  $Re_m = 2000$ . Three-dimensional linear stability analysis was performed on a 2D LDC low  $Re_m$  MHD flow in Ref. 15 to identify the onset of instability. Stable and unstable regions were mapped with respect to the interaction number,  $N = Ha^2/Re$  (up to 30), and Reynolds numbers (up to 7500). Several studies (e.g., Ref. 30) have investigated the critical Reynolds number for Q2D MHD flows.

If  $Ha = 0$ , the flow is 3D. When  $Ha$  is increased, the flow tends to change to Q2D with the Hartmann layers at the walls perpendicular to the magnetic field and the core where the velocity components and the pressure exhibit small variations along the direction of the applied magnetic field.

The effects of  $Re_m$  are less understood. In general, one might expect more unsteadiness, more three-dimensionality (see Ref. 17) and, if  $Re_m$  is increased high enough, dynamo-type physics. These  $Re_m$  effects are investigated in the present work. Also, we want to see how the fundamental properties of the low  $Re_m$  MHD flows such as Hartmann layers and two-dimensionalization are possibly modified at higher  $Re_m$ .

### III. NUMERICAL METHODOLOGY

#### A. Spatial discretization

Grid points are clustered in the Hartmann and Shercliff layers in the liquid near the solid boundaries and at the moving lid using Roberts coordinate transformation (Ref. 31). The mesh is also clustered in the wall to provide the smallest grid cell in the wall to be equal in size to the neighboring cell in the liquid. This non-uniform grid is necessary to both ensure a sufficient number of points in the BLs and resolve the large computational domain efficiently. Each variable is approximated on a fully staggered mesh system as shown in Fig. 2. Velocity and magnetic fields are staggered on the face of the computational cell to avoid checkerboard-type instabilities and to enforce flux conservation. The electric current and electrical

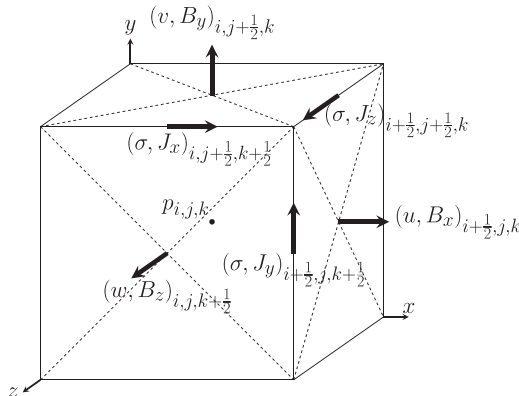


FIG. 2. Staggered variables on computational cell.

TABLE I. Locations of input scalar fields and output derivatives when computed on the staggered computational cell.

Location of input scalar field ( $f$ )	Location of output vector field $\{\partial_x f, \partial_y f, \partial_z f\}$
Cell center	{x-face, y-face, z-face}
Cell corner	{x-edge, y-edge, z-edge}
x-face	{Cell center, z-edge, y-edge}
y-face	{z-edge, cell center, x-edge}
z-face	{y-edge, x-edge, cell center}
x-edge	{Cell corner, z-face, y-face}
y-edge	{z-face, cell corner, x-face}
z-edge	{y-face, x-face, cell corner}

conductivity are located at the computational cell edges. Pressure is located in the center of the computational cell. Second-order spatial accuracy is applied to approximate derivatives using central finite difference schemes and to compute the interpolations between different meshes.

Derivatives are calculated in the following systematic way. The first derivative of a field, positioned on a given location on the computational cell, is always computed from neighboring data. The result is that a field and its first derivative are never collocated (see Table I). The same type of rule is followed with interpolations along the  $x$ ,  $y$ , and  $z$  directions. Ghost points are used as a means to enforce BCs and allow derivative and interpolation operators to behave equivalently in the domain interior as they do in the domain boundaries, which provides operators with convenient commutative properties (Ref. 32). Unknowns are decomposed into interior and boundary values. Second-order boundary treatment is recovered from first-order derivative stencils by adding the remaining derivative stencils, required to recover 2nd-order accuracy, to the right-hand side of the equation (where all source terms are known).

The momentum and induction equations are computed on the computational cell face, while the pressure and correction equations (discussed in Sec. III C 1) are computed on the computational cell center. Additional computational tests were performed using a collocated grid configuration. The following general rules were found to produce consistent results between the staggered and collocated grid configurations. First, the number of interpolations performed to compute terms is minimized—interpolations are only performed when necessary. Second, interpolations are performed such that terms naturally land on the location of the governing equation. For example, the advection term in the induction equation is calculated as follows: (1) the velocity and magnetic fields are interpolated from the cell face to the cell edges; (2)  $\mathbf{u} \times \mathbf{B}$  is then computed on the cell edge; and (3) the curl of  $\mathbf{u} \times \mathbf{B}$  is computed from the cell edges, the result of which is naturally located on the cell face (where the induction equation is computed).

#### B. Ensuring solenoidality of the magnetic field

Enforcing Eq. (5) can be accomplished using one of the several techniques. Two such methods, a constrained transport (CT) method and a projection method, were incorporated in this study and are discussed here. The CT method naturally

satisfies Eq. (5) using a special spatial discretization. The projection method enforces Eq. (5) by estimating a solution and then “projecting” the estimate onto a divergence-free space. Both methods were implemented in MOONS, and their computational time was compared before conducting this study. Trade-offs between the two methods (see Ref. 19) are briefly described here.

The CT method ensures Eq. (5) within machine accuracy at each time step ( $\Delta t$ ) but requires that the magnetic BCs and initial magnetic field distribution are compatible with Eq. (5). The CT method is fast because it requires a single explicit time update but suffers from a diffusion-explicit time step restriction. This limitation becomes prohibitively severe for insulating domains, low  $Re_m$  flows, and very fine grids. The projection method relieves the time step restriction with time-implicit diffusion treatment and is insensitive to initial  $\nabla \cdot \mathbf{B}$  conditions. While the projection method requires matrix inversion, due to implicit diffusion treatment, its computational efficiency was found to be superior to the CT method in most cases. Therefore, the projection method was used for all computations in the present paper. Both method formulations are discussed in more detail below.

### 1. Constrained transport method

The CT method, initially proposed by Ref. 33, prevents the growth of  $\nabla \cdot \mathbf{B}$  intrinsically through a staggered variable conservation scheme (a thorough review is given in Ref. 19). In this discretization, the electric field, magnetic field, and electric current are staggered on the computational cell edge, face, and edge, respectively. A simple proof of how the CT method enforces  $\nabla \cdot \mathbf{B} = 0$  can be derived by writing Faraday’s law, using the mentioned spatial discretization, and updating the magnetic field in time (see Sec. 4.1 in Ref. 19). This derivation reveals a perfect cancellation in the discrete form of  $\nabla \cdot \mathbf{B}$ . This scheme relies on diffusion-explicit treatment, limiting the time step as mentioned above. For the  $Re_m$  range considered in the present work, the CT method was found to require a very small time step, especially with the presence of an outer vacuum region.

### C. Temporal discretization

Equations (1) and (3) are solved separately at each time step. A  $\theta$ -implicit Crank-Nicholson-type method is used for the diffusion terms, a second-order Adams-Bashforth method is used for the advection terms, and pressure is treated purely implicitly. The momentum and induction time-discretized equations, from time level  $n$  to  $n + 1$ , are

$$\frac{\mathbf{u}^{n+1} - \mathbf{u}^n}{\Delta t} - \theta_u Re^{-1} \nabla^2 \mathbf{u}^{n+1} = -\nabla p^{n+1} + \frac{3}{2} \mathbf{K}^n - \frac{1}{2} \mathbf{K}^{n-1},$$

$$\mathbf{K}^n = (1 - \theta_u) Re^{-1} \nabla^2 \mathbf{u}^n + (\mathbf{u}^n \cdot \nabla) \mathbf{u}^n + \frac{Ha^2}{Re} \mathbf{j}^n \times \mathbf{B}^n, \quad (11)$$

$$\frac{\mathbf{B}^{n+1} - \mathbf{B}^n}{\Delta t} + \theta_B Re_m^{-1} \nabla \times (\bar{\sigma}^{-1} \nabla \times \mathbf{B}^{n+1}) = \frac{3}{2} \mathbf{T}^n - \frac{1}{2} \mathbf{T}^{n-1},$$

$$\mathbf{T}^n = -(1 - \theta_B) Re_m^{-1} \nabla \times (\bar{\sigma}^{-1} \nabla \times \mathbf{B}^n) + \nabla \times (\mathbf{u}^n \times \mathbf{B}^n). \quad (12)$$

Here,  $\theta$  is a parameter that controls the degree of explicit-to-implicit treatment of the diffusion terms. Diffusion is treated purely explicitly, centered in time, and exclusively implicitly for  $\theta = 0, 0.5$ , and  $1$ , respectively. Equation (11) is demonstrated to be 2nd-order accurate in time (see Ref. 17). Equations (11) and (12) closely resemble the time discretization used in Ref. 17.

### 1. Fractional-step method

The fractional-step method, or more generally the projection method, is a technique used to solve coupled equations—e.g., velocity and pressure—by decoupling them. The fractional-step method is common in the CFD literature (see, e.g., Refs. 17, 32, 34, and 35) and was first proposed by Chorin in 1968 (see Ref. 36).

A brief overview of how the fractional-step method is applied to Eqs. (11) and (12) and the resulting time-marching procedure are given here. The following discussion is similar to that in Ref. 32, except that the coupled MHD equations are considered here rather than the purely hydrodynamic equations. Therefore, in applying the projection method to the MHD equations, a new scalar field ( $\xi$ ) is introduced to the induction equation to enforce magnetic field conservation.

Equations (11) and (12) can be exactly cast into a matrix form. The matrix operator that includes the diffusion terms and operates on the unknowns ( $\mathbf{u}$ ,  $\mathbf{B}$ ,  $p$ , and  $\xi$ ) can be approximated with a 2nd-order time accurate approximation (see Ref. 32). The advantage of applying this approximation is that the approximated matrix can be factorized, which permits the system of equations to be solved as a sequence of operations. Using discrete gradient ( $G$ ), divergence ( $D$ ), Laplacian ( $\mathcal{L}$ ), and curl ( $C$ ) operators, this sequence of operations may be written as

$$(I - \Delta t \theta_u Re^{-1} \mathcal{L}) \hat{\mathbf{u}} = \mathbf{u}^n + \Delta t \left( \frac{3}{2} \bar{\mathbf{K}}^n - \frac{1}{2} \bar{\mathbf{K}}^{n-1} + BC_1 \right), \quad (13)$$

$$\Delta t \mathcal{L} \zeta^{n+1} = D \hat{\mathbf{u}} - BC_2, \quad (14)$$

$$\mathbf{u}^{n+1} = \hat{\mathbf{u}} - \Delta t G \zeta^{n+1}, \quad (15)$$

$$(I + \Delta t \theta_B Re_m^{-1} C (\bar{\sigma}^{-1} C)) \hat{\mathbf{B}} = \mathbf{B}^n + \Delta t \left( \frac{3}{2} \bar{\mathbf{T}}^n - \frac{1}{2} \bar{\mathbf{T}}^{n-1} + BC_3 \right), \quad (16)$$

$$\Delta t \mathcal{L} \xi^{n+1} = D \hat{\mathbf{B}} - BC_4, \quad (17)$$

$$\mathbf{B}^{n+1} = \hat{\mathbf{B}} - \Delta t G \xi^{n+1}. \quad (18)$$

Here,  $I$ ,  $\hat{\mathbf{u}}$ ,  $\hat{\mathbf{B}}$ ,  $\bar{\mathbf{K}}$ ,  $\bar{\mathbf{T}}$ , and  $BC_{1,2,3,4}$  are the identity matrix, intermediate fields for  $\mathbf{u}$  and  $\mathbf{B}$ , spatially discrete forms of  $\mathbf{K}$ ,  $\mathbf{T}$  in Eqs. (11) and (12), and BCs for  $\mathbf{u}^{n+1}$ ,  $p^{n+1}$ ,  $\mathbf{B}^{n+1}$ , and  $\xi^{n+1}$ , respectively. The scalar field  $\zeta$  enters the equations as a result of the time-splitting error, due to the previously mentioned matrix approximation, and relates to pressure via  $p = \zeta - \theta_u \Delta t Re^{-1} \nabla^2 \zeta$  (see Ref. 32). The  $p - \zeta$  relation holds only in the case that the gradient and Laplacian operators are commutative, which is valid for continuous operators but is not guaranteed for discrete operators. Note that there are no requirements for BCs on  $\hat{\mathbf{u}}$  and  $\hat{\mathbf{B}}$  since BCs for the unknowns have already been absorbed into  $BC_{1,2,3,4}$  (see Ref. 32).

Our procedure in Eqs. (13)–(18) resembles the popular fractional-step method, proposed by Ref. 34, applied to the incompressible momentum and solenoidal induction equations separately. A matrix-free, diagonally preconditioned conjugate gradient (CG) method is used to iteratively solve Eqs. (13)–(18), using 20 iterations for Eqs. (13) and (16) and 5 iterations for Eqs. (14) and (17) at each time level, respectively. If Eq. (16) is solved by a matrix inversion, then the matrix to be inverted has a complicated structure due to the non-uniform grid, variable electrical conductivity and staggered magnetic field configuration, resulting in *slanted* non-zero elements (see Fig. 3). The advantages of the matrix-free method include ease of implementation and less computational memory consumption compared to storing the entire curl-curl operator. The disadvantage, however, is that the matrix-free method is less computationally efficient as storing the curl-curl operator—one test performed resulted in a  $\sim 5\%$  difference in computational time.

Due to the stiffness in Eq. (16) and numerical tests yielding faster and more stable computations for time-implicit diffusion treatment,  $\theta_u = 1$  and  $\theta_B = 1$  were used exclusively in this study.

#### D. Modeling the infinitely large computational domain

The computational domain consists of the conducting LM, conducting wall, and vacuum domains. In the present study, a sufficiently large computational vacuum domain is used to model an infinitely large one. The size is large enough when, as the domain is further increased in size, the solution no longer significantly changes. The size of the vacuum domain can be estimated using Eq. (8). The equation reveals that the induced magnetic field strength decays proportionally to  $Re_m/|r|^3$  in vacuum sufficiently far from the conductor. So, the size of the domain should be roughly proportional to  $Re_m$ . In this paper, the domain size was tested for  $Re_m = 1000$  in light of this information.

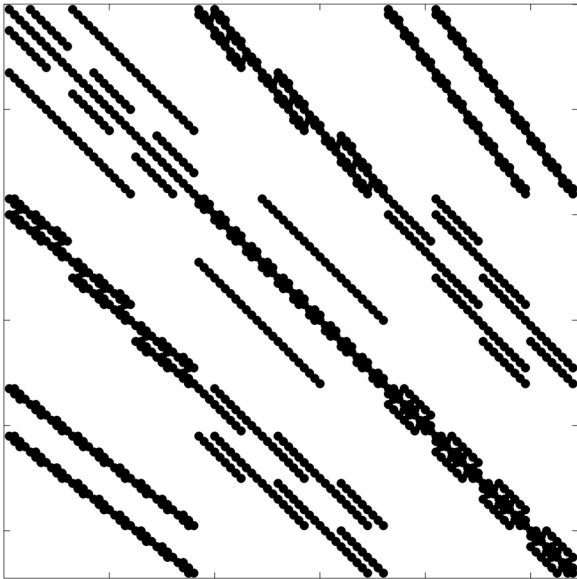


FIG. 3. Matrix visualization (non-zero elements) of curl-curl operator Eq. (16).

The MHD LDC flow was simulated at  $Re_m = 1000$  using total domain sizes of volumes  $\{\Omega_{t,1}, \Omega_{t,2}, \Omega_{t,3}, \Omega_{t,4}\} = \{3.5^3, 7^3, 14^3, 28^3\}$ . The percent difference in the total kinetic energy between  $\Omega_{t,1}$  and  $\Omega_{t,2}$ ,  $\Omega_{t,2}$  and  $\Omega_{t,3}$ , and  $\Omega_{t,3}$  and  $\Omega_{t,4}$  was 0.31%,  $5.4 \times 10^{-4}\%$ , and  $6.5 \times 10^{-5}\%$ , respectively. The final chosen total domain size was that of volume  $14^3$  and is used for the remainder of this study.

#### E. Modeling the multi-material domain

In general, the computational domain includes three electrical conductivities for the liquid, electrically conducting wall, and vacuum. In fact, the electrical conductivity of the vacuum domain in the computations is not set to zero but to a small enough value to prevent electrical currents from leaving the conducting domain. The computational domain is, therefore, a multi-material structure, resulting in the conductance ratio that may vary by several orders of magnitude. The need to simulate the magnetic field in the vacuum results in a poorly conditioned system when solving Eq. (3) since  $\bar{\sigma}$  dramatically changes across the conductor-insulator interface. This feature requires a special treatment of the diffusion term in the induction equation to avoid unphysical solutions that might appear due to non-conservative flux approximations at the material interfaces (see Ref. 37). The electrical conductivity is kept inside the derivative to perform this particular diffusion term treatment and maintain a conservative scheme.

#### F. Testing the code

Several tests, some of which were already performed in Ref. 38, are briefly summarized here. Purely hydrodynamic LDC flows between  $400 \leq Re \leq 1000$  showed excellent matches with existing numerical data. Low  $Re_m$  conducting and insulating duct MHD flows, and a LDC MHD flow, all showed an excellent match up to Hartmann 15 000 with analytic solutions and numerical data, respectively. A finite  $Re_m$  MHD periodic channel flow showed an excellent match at high Hartmann numbers and a fair match at low Hartmann numbers with existing numerical data. Also, a 1D finite  $Re_m$  MHD channel flow, induced by a constant and transversely applied magnetic field and a constant, time-varying applied magnetic field, was compared at steady state, and an excellent match was found with analytic solutions. All computations qualitatively and quantitatively agree with analytic solutions and existing numerical data.

### IV. RESULTS AND DISCUSSION

#### A. Selecting the electrical conductivity of the insulating outer domain

The electrical conductivity of the outer domain,  $\bar{\sigma}_v$ , is ideally zero, but because Eq. (3) is solved continuously across  $\Gamma_c$ ,  $\bar{\sigma}_v$  cannot be set to zero because it appears in the denominator. Moreover, the computational effort is increased as  $\bar{\sigma}_v$  becomes more discontinuous across  $\Gamma_c$ . Therefore, the largest  $\bar{\sigma}_v$  approaching zero must be determined such that the solution no longer significantly changes as  $\bar{\sigma}_v$  is further decreased. The preliminary study to identify a suitable  $\bar{\sigma}_v$  was performed at  $Re_m = 1000$ . The high  $Re_m$  case was used because the induced

magnetic field would likely reach far into  $\Omega_v$ . Performing computations at very low  $\bar{\sigma}_v$  would not have been possible with explicit time-marching because the stiffness of the matrix to be inverted in Eq. (12) becomes too severe. As  $\bar{\sigma}$  becomes more discontinuous across  $\Gamma_c$ , the matrix inversion in Eq. (12) becomes increasingly ill-conditioned, greatly benefits from preconditioning, and requires tens of iterations to converge. Changing from explicit to implicit time-marching still requires tens of iterations to solve Eq. (12) at each time step, but the time step restriction is significantly relieved. For example, the time step was relieved by four orders of magnitude for  $\bar{\sigma}_v = 10^{-4}$  and resulted in considerably faster computations.

Equations (13)–(18) are solved until the velocity and magnetic fields reached a steady state. To determine when a steady state is reached, the integral dimensionless kinetic energy  $E_u$  and induced magnetic field energy  $E_{B^1}$  were monitored as a function of time,

$$E_u(t) = \int_{\Omega_f} E_K d\Omega, \quad E_K = \frac{1}{2} \mathbf{u} \cdot \mathbf{u}, \quad (19)$$

$$E_{B^1}(\Omega^*, t) = \int_{\Omega^*} E_M d\Omega, \quad E_M = \frac{1}{2} A |B^1 \cdot B^1|. \quad (20)$$

Here,  $\Omega^*$ ,  $A l = Ha^2 / (Re Re_m)$ ,  $E_K$ , and  $E_M$  are the domain of integration, Alfvén number, and local dimensionless kinetic and magnetic energy, respectively. The Alfvén number estimates the ratio of magnetic to kinetic energy. In addition, the integral dimensionless Joule heating was computed,

$$E_j(\Omega^*, t) = \int_{\Omega^*} E_J d\Omega, \quad E_J = \frac{Ha^2 j^2}{Re \bar{\sigma}}. \quad (21)$$

Here,  $E_J$  is the Joule heating.  $E_u$ ,  $E_{B^1}$ , and  $E_j$  can be directly compared because they all require the multiplication of the same physical scale,  $\rho U^2 L^3$ , to recover energy in Joules. The steady-state percent difference between  $E_{B^1}(\Omega_f, t)$  at  $\bar{\sigma}_v = 4 \times 10^{-3}$ ,  $2 \times 10^{-3}$ ,  $1 \times 10^{-3}$ , and  $5 \times 10^{-4}$  was 2.3%, 1.2%, and 0.4%, respectively (see Fig. 4). From here on,  $\bar{\sigma}_v = 10^{-3}$  was used for the vacuum domain.

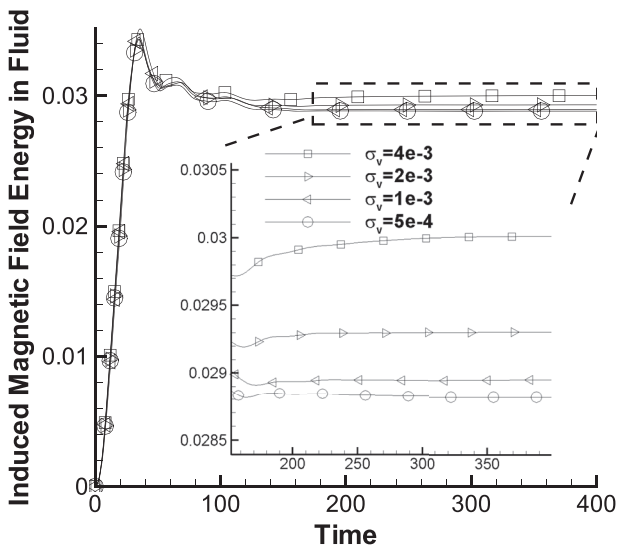


FIG. 4. Effect of the electrical conductivity of the insulating outer domain on the computed magnetic energy.

## B. Mesh independence study

Additionally, a mesh refinement study has been conducted to ensure that a sufficient number of grid points were used to resolve the flow and accurately depict the energy of the system. These tests were carried out at  $Re_m = 200$  with four grid resolutions: coarse  $N_{cells} = 51$  and 840, medium  $N_{cells} = 278$  and 528, and two fine grids  $N_{cells} = 1, 614$ , and 720 and  $N_{cells} = 10, 264$ , and 320. Cells were concentrated near the cavity walls where the BLs are formed and at the moving lid, due to the velocity discontinuity at the intersection of the stationary walls and moving lid. The steady-state percent difference in integral kinetic and magnetic energies between the second finest and finest grids was 0.66% and 1.1% (see Fig. 5), respectively. The second finest grid was used for the remainder of this study.

## C. Steady to unsteady flow comparison

Initially, the flow is at rest, and the induced magnetic field is zero everywhere. As the lid starts moving, the fluid starts circulating around the cavity and induces a magnetic field whose distribution and magnitude change in time until the velocity and the induced magnetic field reach a steady state. Steady-state velocity and induced magnetic field distributions will exist or not exist depending on  $Re_m$ ,  $Ha$ ,  $Re$ , and  $c_w$ . Also, we caution that due to the possibility of hysteresis (see Ref. 17), the uniqueness of the solution is not in general guaranteed for finite  $Re_m$  MHD flows, but here, only one solution is observed. Steady-state solutions are more likely to exist at lower  $Re$ , lower  $Re_m$ , and higher  $Ha$ . This fluid flow regime is typically characterized as being laminar, with a small induced-to-applied magnetic field ratio, and strong damping effect on the flow due to Joule dissipation that occurs mostly in the Hartmann layers and in the walls.

For unsteady or transitioning MHD flows, there are three time scales if the flow is inductionless and four time scales in the case of finite  $Re_m$ . These convective, diffusive, Hartmann damping, and magnetic diffusion times are  $t_c = L/U$ ,  $t_v = L^2/\nu$ ,  $t_j = \rho/(\sigma_l B^2)$ , and  $t_m = L^2 \sigma_l \mu_m$ , respectively (see Refs. 29 and 39). The convective, or eddy turn-over, time estimates the time for the largest scale eddy to perform a full 360° revolution. The diffusion time is the time for momentum to diffuse a distance  $L$  in a single diffusive time unit. The Hartmann damping time is the time for the magnetic field to change the

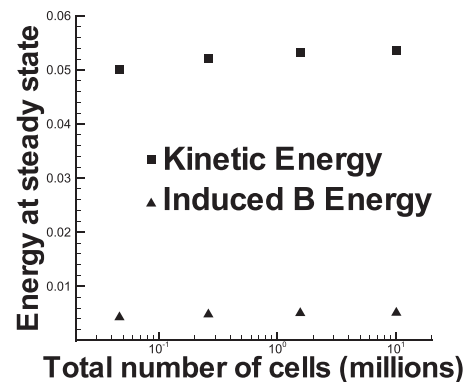


FIG. 5. Grid independence study at  $Re_m = 200$ .

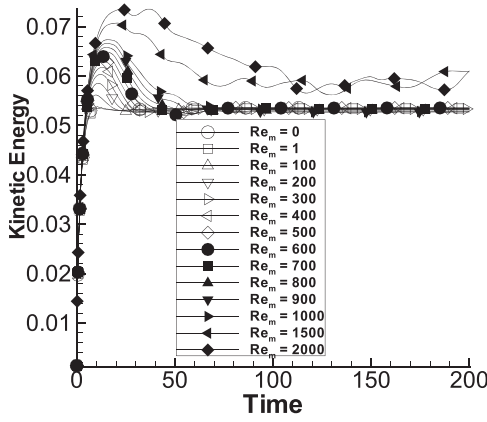


FIG. 6. Kinetic energy over time.

originally three-dimensional flow to a Q2D configuration. The magnetic diffusive time, or resistive decay time, is the time for the magnetic field to diffuse a distance  $L$  in a single magnetic diffusive time unit.

In the present context of finite  $Re_m$  MHD flows, the effect of increasing  $t_m$  by increasing  $Re_m$  is of particular interest. This effect is shown in Figs. 6 and 7 in the form of the kinetic and magnetic energy versus time using  $Re_m$  as a parameter. First, the integral kinetic energy increases from zero to a local maximum, then decreases, and saturates to an asymptotic steady-state value. Interestingly, the steady-state kinetic energy is nearly the same across almost all  $Re_m$  range despite an increasing difference in the kinetic energy with increasing  $Re_m$  during the transition period (Fig. 6). Obviously, the flow reaches a steady state more quickly at low  $Re_m$ . This agrees with observations seen in kinematic MHD studies at  $Re_m = 1000$  by Ref. 29. Despite having nearly the same steady-state integral kinetic energy, the steady-state velocity and magnetic field distributions vary across the range of  $Re_m$ , as will be shown in later sections. This suggests that at  $Re_m \lesssim 1000$ , the integral kinetic energy serves as an invariant in this MHD LDC flow problem. At the highest  $Re_m$  of 1500 and 2000 in the study, the steady state was not achieved such that the effect of  $Re_m$  on the integral kinetic energy was always present.

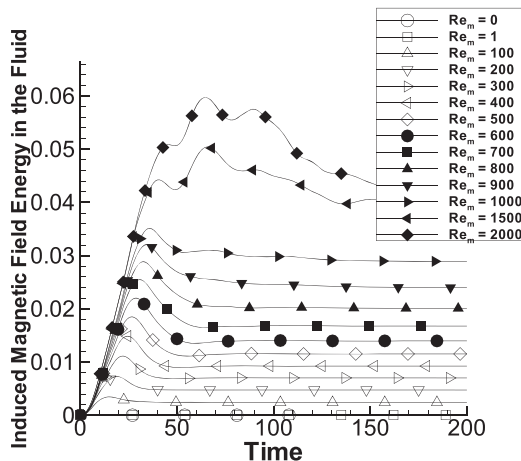
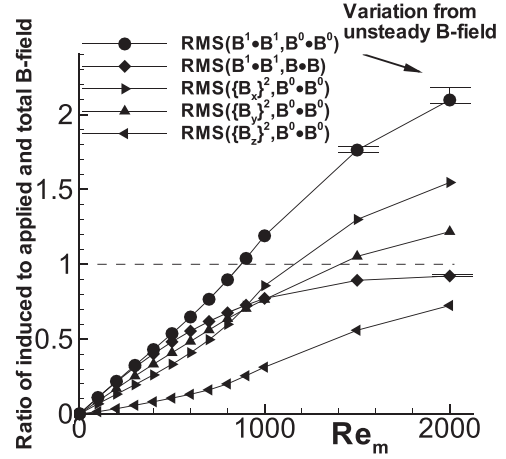


FIG. 7. Induced magnetic field energy over time.

FIG. 8. Ratio of steady-state induced to applied magnetic field energy vs.  $Re_m$ .

The behavior of the integral magnetic field energy as  $Re_m$  increases is different (Fig. 7). The magnetic field energy is always dependent on  $Re_m$  regardless of whether the flow reaches a steady state or is in a transitional phase. The temporally asymptotic integral induced magnetic field energy in the fluid and its components are plotted in Fig. 8 versus  $Re_m$  in the form of a Root-Mean-Square (RMS), scaled by either the total or applied magnetic field. The RMS is computed using the following formula:

$$RMS(\chi, \Upsilon) = \frac{\sqrt{\int_{\Omega_{fluid}} \chi d\Omega}}{\sqrt{\int_{\Omega_{fluid}} \Upsilon d\Omega}}. \quad (22)$$

Here,  $\chi$  and  $\Upsilon$  are dummy scalar fields. Figure 8 clearly demonstrates that the magnetic field behavior is nearly linear in a range of  $Re_m$  up to roughly 500 and then begins to resemble an exponential growth. Another useful observation is that the induced magnetic field reaches the magnitude of the applied one at  $Re_m \approx 850$ . Interestingly, the non-linear behavior and unsteadiness also become pronounced at about the same  $Re_m$ , possibly indicating that the most substantial modifications of the flow start as soon as the induced and applied magnetic fields become nearly equal.

#### D. Applicability of the inductionless approximation

In the MHD flows where the  $Re_m$  is small, the induced magnetic field is small and can be neglected compared to the applied one. Also, convection of the magnetic field is negligibly small compared to diffusion and can be neglected. In such conditions, the governing equations are simplified to the inductionless form as briefly discussed in Sec. I. The applicability of the inductionless approximation depends on the magnitude of  $Re_m$ . Typically, the inductionless approximation is valid if  $Re_m \ll 1$  (see Refs. 17 and 40). However, some authors claim that accurate results can be obtained using the inductionless approximation even for  $Re_m$  of the order of unity (see Refs. 40 and 41). The results of the present study demonstrate that for the reference MHD LDC flow, the range of applicability of the inductionless approximation depends on whether or not the flow is in a steady state. For unsteady flows, as

shown in Sec. IV C, the effect of  $Re_m$  on the flow can be neglected only if  $Re_m \ll 1$ . If the flow reaches the steady state, the situation is different. Namely, the steady-state integral kinetic energy becomes independent of the  $Re_m$  for even high  $Re_m \sim 10^2$ , while the induced magnetic field changes linearly with  $Re_m$  values up to  $\sim 500$ . This may suggest that the inductionless approximation is still valid, but this idea cannot be fully justified without looking carefully at the distributions of the velocity, induced magnetic field, and induced currents. This was done in the present section for  $Re_m \ll 1$ ,  $Re_m = 1$ , 100, 500, and 1000, for which the solution had converged to the steady state.

The effect of  $Re_m$  on the steady-state velocity distributions as a function of  $x$  and  $y$  is illustrated in Fig. 9. Clearly, for  $0 < Re_m < 100$ , the effect of  $Re_m$  is very small. In fact, differences between velocity curves plotted at  $Re_m \ll 1$  and  $Re_m = 1$  are nearly indistinguishable, and differences between  $Re_m = 1$  and  $Re_m = 100$  are very small. Significant changes in both  $u$  and  $v$  velocity components are, however, seen at  $Re_m = 500$  and 1000. The  $u$  component has a larger overshoot at higher  $Re_m$  compared to lower  $Re_m$  near the lid [Fig. 9(a)]. The  $v$  component of velocity is more oscillatory along the  $x$ -direction [Fig. 9(c)] at higher  $Re_m$  values compared to lower ones.

A normalized induced magnetic field was computed,  $\beta^1 = \frac{\mathbf{B}^1 - \min(\mathbf{B}^1)}{\max(\mathbf{B}^1) - \min(\mathbf{B}^1)}$ , to compare the relative values of the distributions at various  $Re_m$ . Due to anti-symmetry of the  $x$  and  $y$  components of the magnetic field, and the existence of a steady solution, the minimum and maximum are equal with opposite

sign [ $\min(B_x) = -\max(B_x)$  and  $\min(B_y) = -\max(B_y)$ ]. The shape of the magnetic field distribution does not significantly change between  $Re_m \ll 1$  and  $Re_m = 100$  [Figs. 10(a), 11(a), 12(a), 10(b), 11(b), and 12(b)], suggesting a solution with pronounced self-similarity. However, the magnetic field distribution does change shape at larger  $Re_m$  values [Figs. 10(c), 11(c), 12(c), 10(d), 11(d), and 12(d)], indicating a change in electric current paths and the transition out of the self-similar solution regime.

Similar trends were observed in the distributions of the induced electric current in Figs. 13 and 14. The  $x$  and  $y$  components of electric current along the  $x$  and  $y$  directions have very complicated distributions and follow very similar behavior for  $0 < Re_m < 100$  cases [see Figs. 13(a)–13(d)]. The  $x$  and  $y$  components of electric current are nearly zero in the fluid domain along the  $z$  direction but are significantly larger in the conducting walls [Figs. 14(a) and 14(b)]. The  $z$  component of electric current varies quite rapidly, even between  $Re_m \ll 1$  and  $Re_m = 100$ , along the  $z$  direction [Fig. 14(c)] demonstrating one or two inflection points depending on  $Re_m$ . However, the sensitivity of the electric current distribution with respect to  $Re_m$  may be high due to the low magnitude of the electric current in this particular cut-line.

To conclude this section, it appears that the inductionless approximation is applicable in the range  $0 < Re_m \lesssim 100$ , provided that the flow is in steady state. In this range, the  $Re_m$  has almost no effect on the velocity field and induced electric current distributions, while the induced magnetic field demonstrates similarity and changes linearly in magnitude with  $Re_m$ .

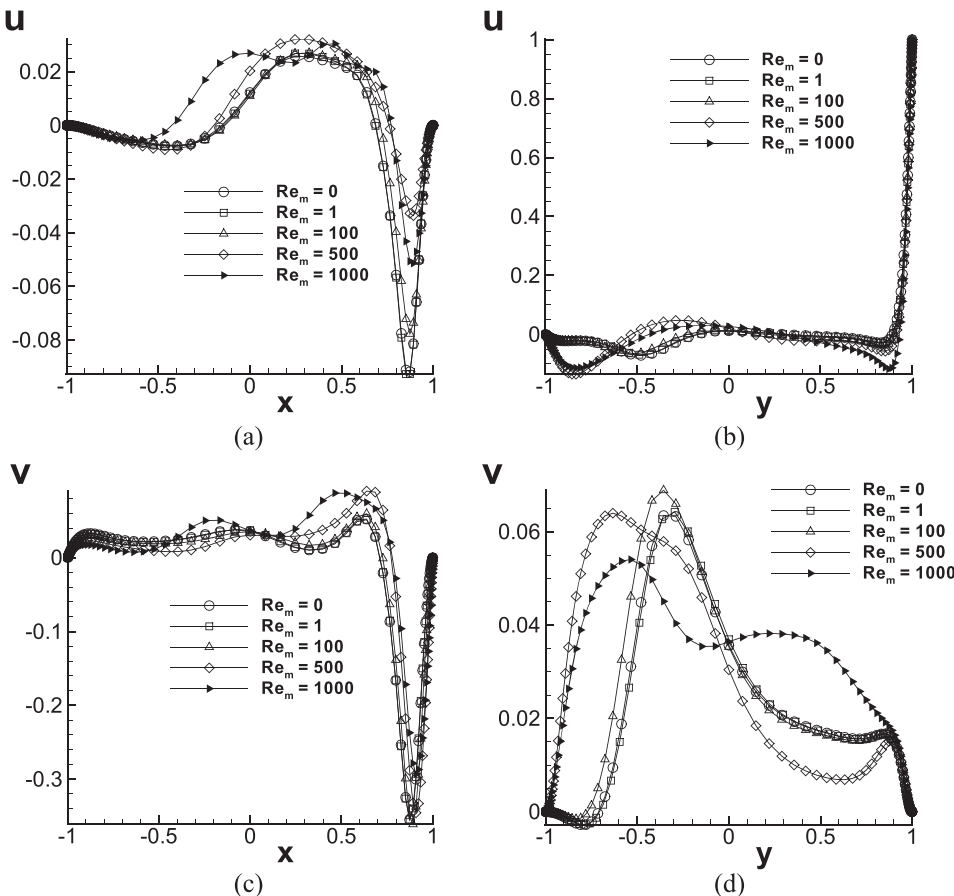


FIG. 9. The  $u$  component of velocity along the  $x$  (a) and  $y$  (b) directions and  $v$  component of velocity along the  $x$  (c) and  $y$  (d) directions in the cavity center.

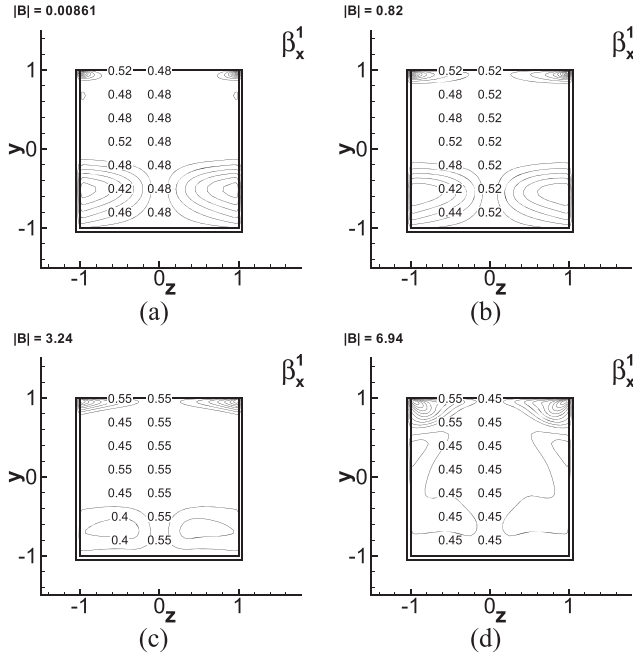


FIG. 10. The  $x$  component of the normalized induced magnetic field contours at  $x = 0$  for (a)  $Re_m \ll 1$ , (b)  $Re_m = 100$ , (c)  $Re_m = 500$ , and (d)  $Re_m = 1000$ .

### E. Two-dimensionality

The tendency of low  $Re_m$  MHD flows to become Q2D under the influence of a strong magnetic field is well known (see Ref. 42); however, whether or not the same tendency remains at higher  $Re_m$ , compared to inductionless flows, is not clear, neither in general nor in the particular case of the MHD LDC flow. Typically, at  $Re_m \ll 1$ , applying a strong magnetic field to a wall-bounded flow results in flattening of the velocity profile along the magnetic field lines, suppression of the velocity component in the direction of the

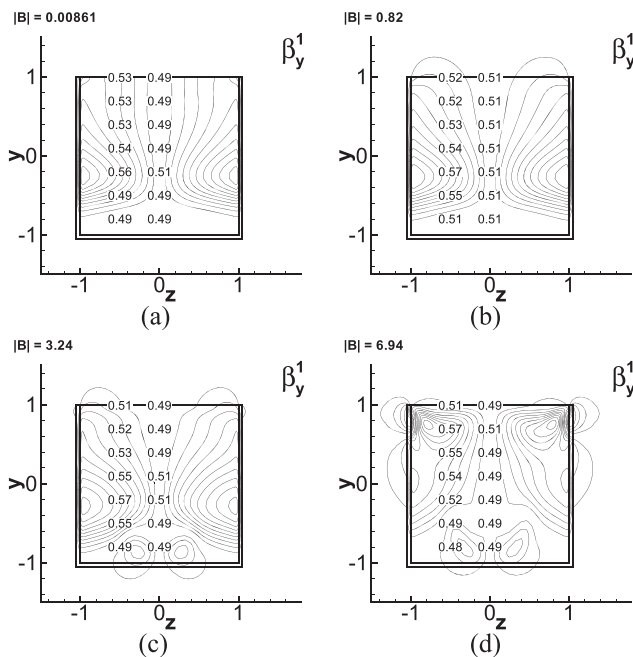


FIG. 11. The  $y$  component of the normalized induced magnetic field contours at  $x = 0$  for (a)  $Re_m \ll 1$ , (b)  $Re_m = 100$ , (c)  $Re_m = 500$ , and (d)  $Re_m = 1000$ .

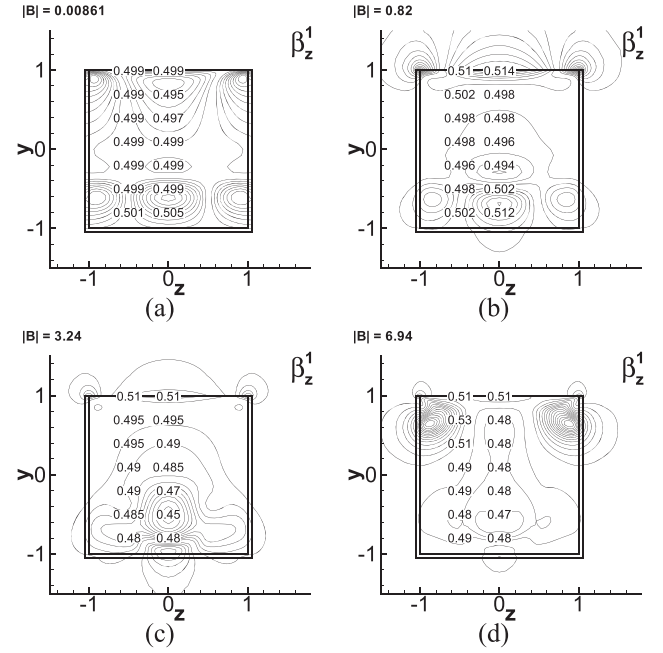


FIG. 12. The  $z$  component of the normalized induced magnetic field contours at  $x = 0$  for (a)  $Re_m \ll 1$ , (b)  $Re_m = 100$ , (c)  $Re_m = 500$ , and (d)  $Re_m = 1000$ .

applied magnetic field, and formation of thin boundary Hartmann layers. The thickness of the Hartmann layer at the walls perpendicular to the applied magnetic field scales as  $1/Ha$ . Eventually, if the magnetic field is strong enough, such a flow exhibits a 2D core where the velocity is fairly uniform, while the 3D effects are localized within a small portion of the flow, including the BLs at the flow confining walls and possibly in thin internal shear layers. At high or even moderate  $Re_m$ , the induced magnetic field becomes comparable with the applied one and can even exceed the applied field as demonstrated in the present study (Fig. 8). Obviously, the Q2D flow structure typical to low  $Re_m$  flows is no longer necessarily compatible with the electric current, magnetic field, and associated Lorentz force distributions at sufficiently higher  $Re_m$  as more complex flow features might be expected.

Present computations for the MHD LDC flow clearly indicate that as  $Re_m$  increases, the flow becomes more three-dimensional [Figs. 15(c), 15(d), 16(c), 16(d), 17(c), 17(d), and 18]. This effect is in agreement with two-dimensionalization due to decreasing  $Re_m$  in turbulent duct MHD flows at finite  $Re_m$  seen in Ref. 17. In the present study, the local two-dimensionality was measured by computing a parameter  $P_{2D} = |\mathbf{u} - \mathbf{u}_{center}|$ , where  $\mathbf{u}_{center}$  is the velocity at the cavity center (the  $z = 0$  plane) and is a function of  $x$  and  $y$ .  $P_{2D}$  was plotted as a function of  $z$  at  $x = 0$  and  $y = 0$  in Figs. 19(a)–19(c). Results show that the flow is mostly two-dimensional when  $Re_m = 0$  and becomes more three-dimensional as  $Re_m$  increases.

The two-dimensionality at low  $Re_m$  can also be observed via the induced magnetic field. From the central plane in the  $x$ -direction of the driven cavity flow, the induced magnetic field appears similar to that in two duct flows in opposing directions [Figs. 10(a) and 10(b)], and from this, the two-dimensionality can clearly be observed. Similar to the

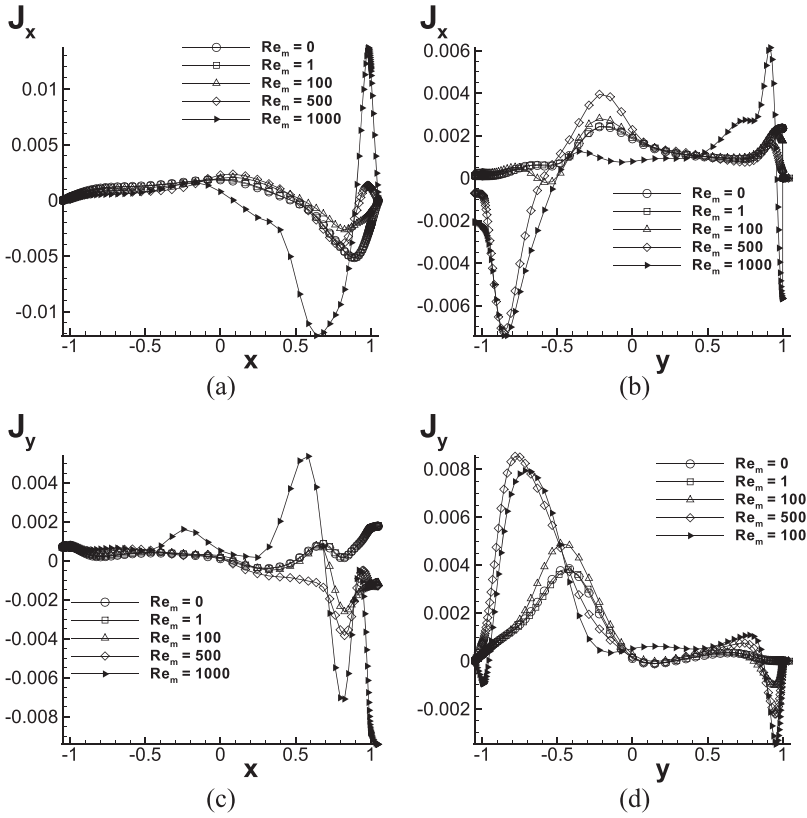


FIG. 13. The  $x$  component electric current along the  $x$  (a) and  $y$  (b) directions and  $y$  component electric current along the  $x$  (c) and  $y$  (d) directions in the cavity center.

velocity field, the induced magnetic field shows more three-dimensionality [Figs. 10(c) and 10(d)] at  $Re_m$  higher than  $\sim 100$ .

Formation of Hartmann layers is another peculiarity of wall-bounded MHD flows at low  $Re_m$ . The  $v$  component of velocity, plotted along  $z$  at  $x = 0$  and  $y = \pm 0.8$  in Figs. 20(a)

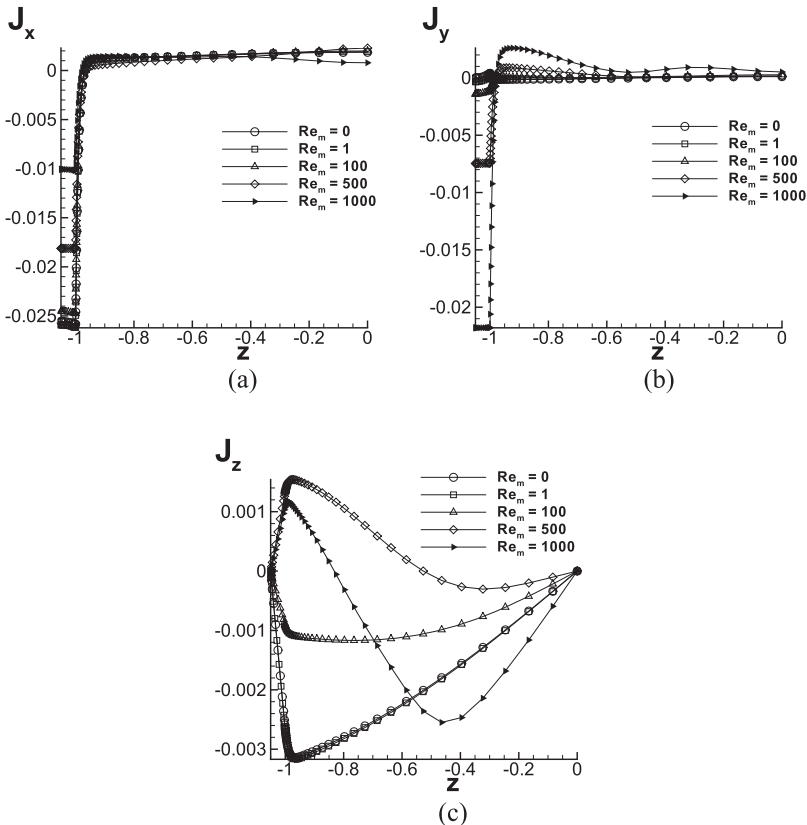


FIG. 14. The  $x$  (a),  $y$  (b), and  $z$  (c) components of electric current along the  $z$  direction in the cavity center for half of the domain.

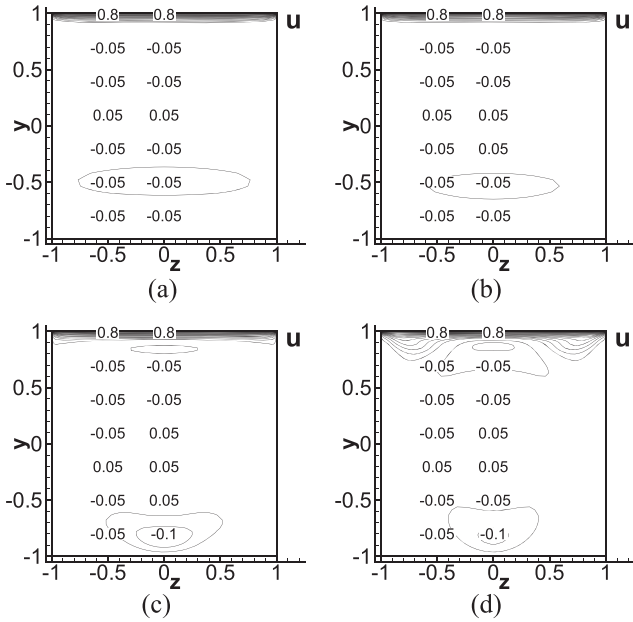


FIG. 15. The  $u$  component of velocity contours at  $x = 0$  for (a)  $Re_m \ll 1$ , (b)  $Re_m = 100$ , (c)  $Re_m = 500$ , and (d)  $Re_m = 1000$ .

and 20(b), respectively, demonstrates the classic MHD velocity profile with a uniform core and distinctive Hartmann layers for  $0 < Re_m \lesssim 100$ . While a Hartmann BL still seems to exist at the wall for higher  $Re_m$  cases, due to the no-slip condition, the distribution in the center of the cavity no longer resembles a “core flow.” As a result, it is difficult to draw general conclusions about how the Hartmann BL is affected by the change in  $Re_m$  in the range presented.

#### F. Frozen magnetic field lines and flux expulsion

In the high  $Re_m$  limit, the total magnetic field becomes *frozen* to the velocity field and, therefore, magnetic field

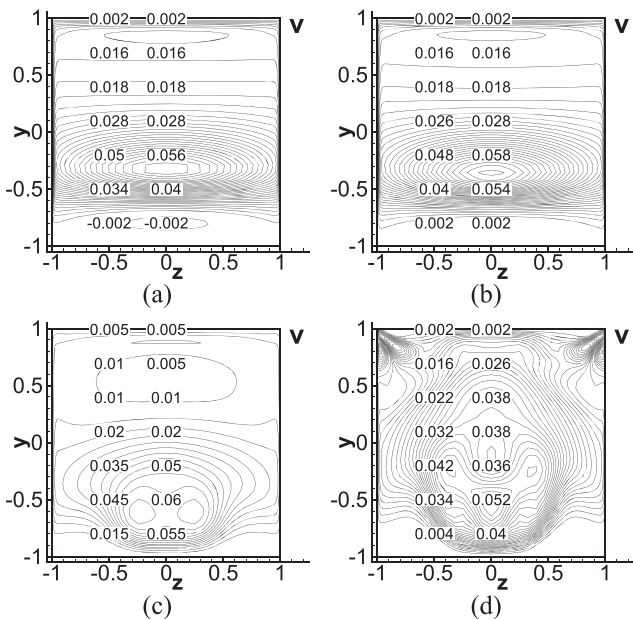


FIG. 16. The  $v$  component of velocity contours at  $x = 0$  for (a)  $Re_m \ll 1$ , (b)  $Re_m = 100$ , (c)  $Re_m = 500$ , and (d)  $Re_m = 1000$ .

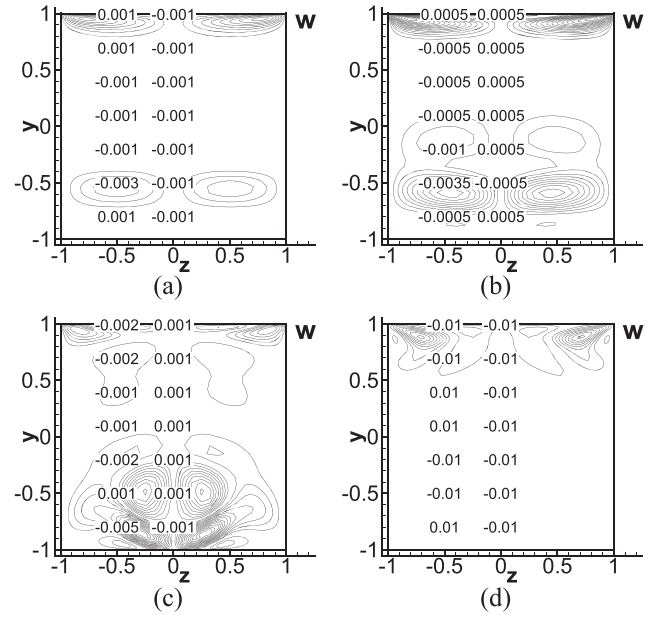


FIG. 17. The  $w$  component of velocity contours at  $x = 0$  for (a)  $Re_m \ll 1$ , (b)  $Re_m = 100$ , (c)  $Re_m = 500$ , and (d)  $Re_m = 1000$ .

lines become purely tangential at the driving lid (see Ref. 1). This trend is clearly observed in the present computations as shown in Fig. 21, where total magnetic field lines are traced in a grid of  $10 \times 10$  points at  $z = -1.05$  and follow the path to the other end of the cavity at  $z = 1.05$ . Naturally, in Fig. 21(a), the induced magnetic field strength is negligible at  $Re_m \ll 1$ , so the total applied magnetic field lines pass straight through the cavity. Alternatively, at higher  $Re_m$ , in Figs. 21(b)–21(d), the induced magnetic field is non-zero and distorts the total magnetic field lines as they pass through the cavity. Expectedly, the severity of the magnetic field line stretching is proportional to  $Re_m$ . Interestingly, stretching of the total magnetic field lines appears to be most apparent near the  $(x, y) = (1, -1)$  corner at  $Re_m = 100$ , rather than regions of largest velocity (near the lid).

It is noteworthy that the  $z$  component of the induced magnetic field is primarily negative in the fluid domain [Figs. 22(a), 22(b), and 23(c)]. This negative magnitude of the induced magnetic field conceptually agrees with the magnetic flux expulsion at high  $Re_m$ , where the total magnetic field is expelled from the moving conducting fluid. Even at high  $Re_m$ , the  $z$  component of the induced magnetic field only reaches approximately  $-0.2$ , which is only 20% of full expulsion (of  $B_z^1 = -1$ ) in the fluid domain.

#### G. Magnetic field penetration into the vacuum

The induced magnetic field can penetrate far beyond the conductor and even into the vacuum. The depth at which the induced magnetic field penetrates into the vacuum is of interest because this provides useful information about the validity range of approximate local magnetic BCs, in particular of the PV BCs as discussed in this paper earlier. In the case of a dipole magnetic field, very far from the center of the dipole, the field strength decreases with the inverse-cube of the

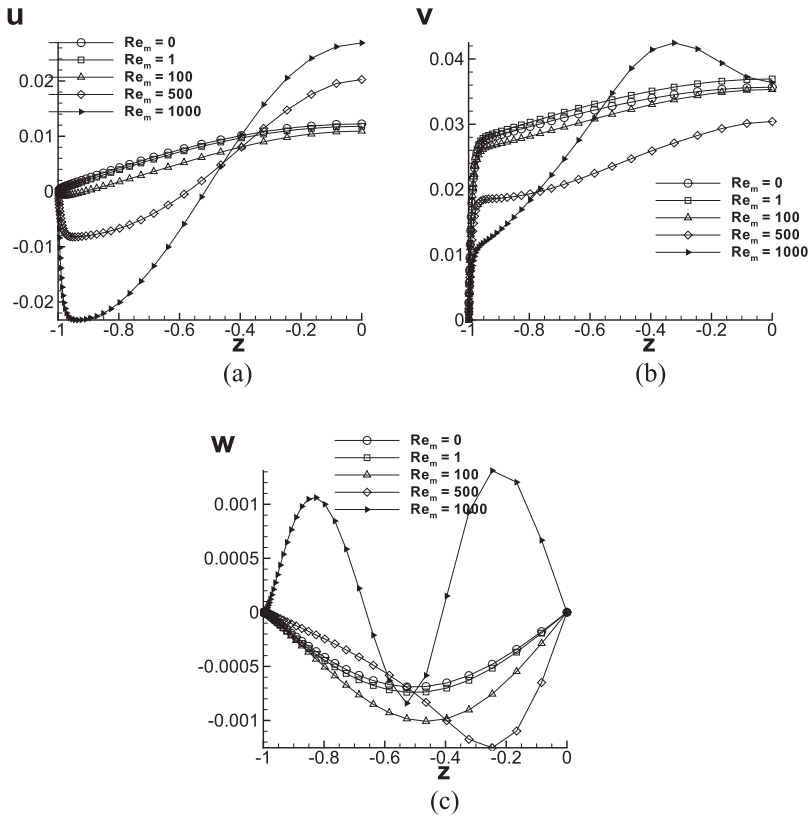


FIG. 18. The  $u$  (a),  $v$  (b), and  $w$  (c) components of velocity along the  $z$  direction in the cavity center for half of the domain.

distance ( $1/|r|^3$ ) but may differ for more complicated magnetic field distributions as in the reference case of the MHD LDC flow.

The farther the magnetic field penetrates into the vacuum, the larger the computational domain must be to satisfy the physically accurate far-field magnetic BCs  $\mathbf{B}^1 = 0$

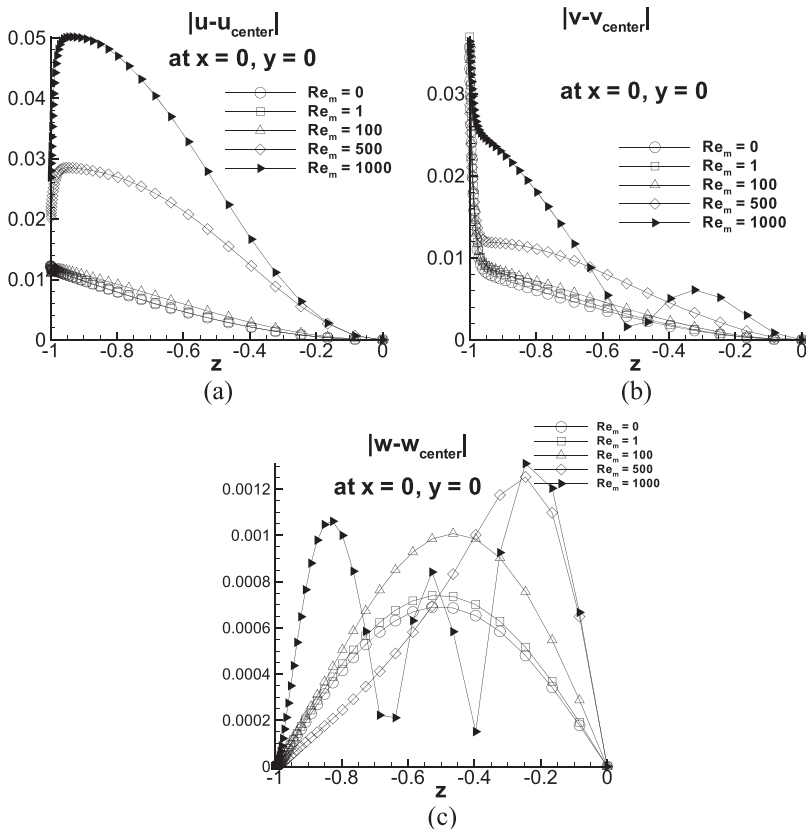


FIG. 19. The two-dimensionality parameter  $P_{2D}$  of the  $u$  (a),  $v$  (b), and  $w$  (c) components of velocity along the  $z$  direction in the cavity center for half of the domain.

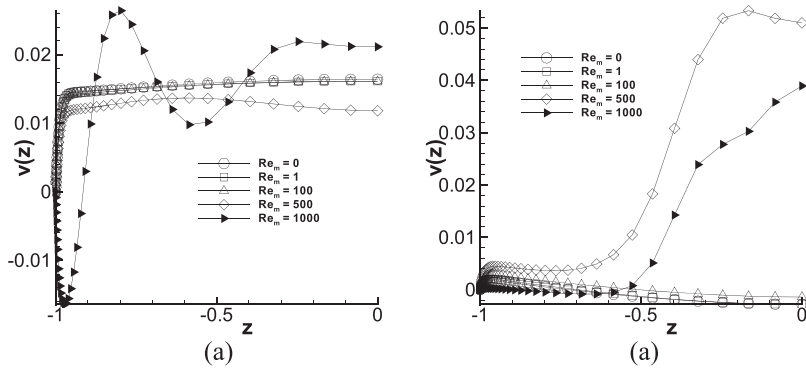


FIG. 20. The  $v$  component of velocity near along the  $z$  direction at  $y = 0.8$  (a) and  $y = -0.8$  (b) in the cavity center for half of the domain.

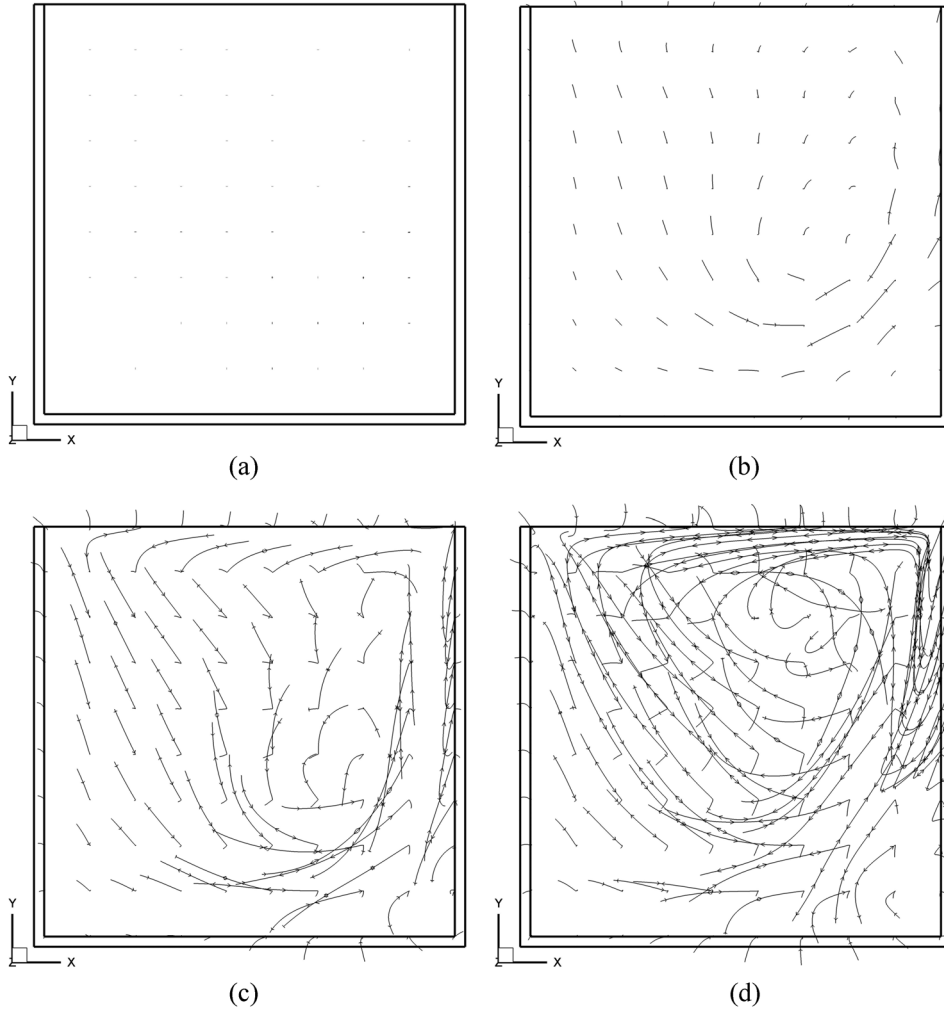


FIG. 21. Total magnetic field lines traced in a grid of  $10 \times 10$  points from  $z = -1.05$  to  $z = 1.05$ , along the applied magnetic field direction for (a)  $Re_m \ll 1$ , (b)  $Re_m = 100$ , (c)  $Re_m = 500$ , and (d)  $Re_m = 1000$ . The magnetic field lines begin to become frozen to the flow as  $Re_m$  increases.

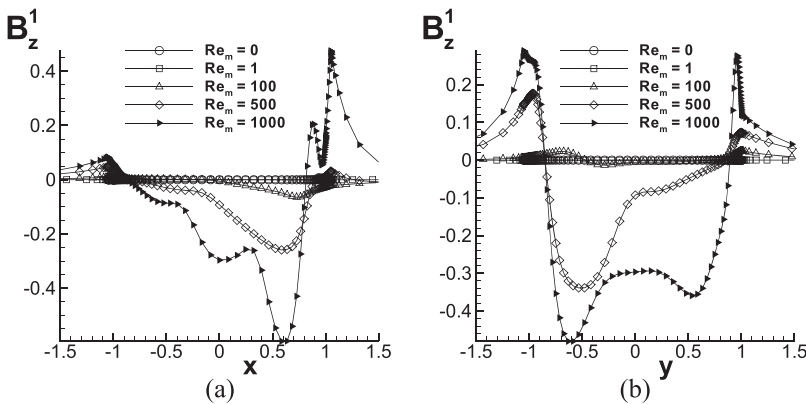


FIG. 22. Magnetic field distributions along the  $x$  (a) and  $y$  (b) directions in the cavity center.

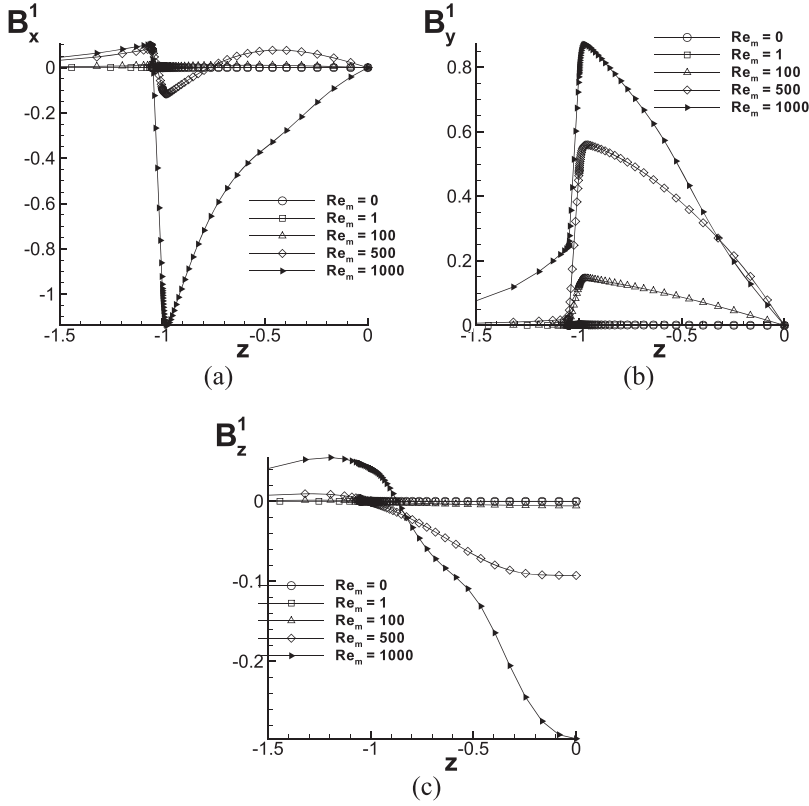


FIG. 23. The  $x$  (a)  $y$  (b), and  $z$  (c) components of magnetic field along the  $z$  direction in the cavity center for half of the domain.

at “infinity.” Furthermore, there is interest in *how* the magnetic field penetrates into the vacuum and what is the amount of energy associated with the magnetic field penetrating into the vacuum domain. That is, the induced magnetic field has interface-normal and tangential components, while the tangential component is fully ignored in the approximate PV BCs. Therefore, the ratio of tangential to perpendicular components of the induced magnetic field across the interface is of interest to better understand the range of validity of approximate induced magnetic field BCs against the full RV BCs.

First, we analyzed the decay of the induced magnetic field in vacuum. The  $1/|r|^3$  decay of the induced magnetic field in the vacuum domain was confirmed using a least-square fit of the induced magnetic field magnitude along the  $x$ -direction, which resulted in exponents (3.22, 3.15, 3.13, 3.13, 3.16, 3.21, 3.29, 3.41, 3.54, and 3.52) for  $Re_m = 100, \dots, 1000$ , respectively. This result suggests that the induced magnetic field in the reference LDC problem is of a dipole type and confirms that our model of the physical system is accurately capturing the decay of the induced magnetic field. Furthermore, this is additional evidence that the domain size used is sufficiently large such that formulating the magnetic field BC at the boundaries of a truncated domain does not disturb the induced magnetic field nor the velocity distribution in the flow domain.

#### H. Energy balance and distribution as $Re_m$ increases

The only power input to the system is via the shear-driven lid (Ref. 43),

$$\mathcal{P} = \int_{\Gamma_{lid}} u \tau_w d\Gamma. \quad (23)$$

Here,  $\tau_w = Re^{-1} \partial_y u$  is the driving lid shear stress. Therefore, the power input depends on  $Re$  and  $\partial_y u$  (i.e., depends on the solution) and is therefore variable in time and space on the driving lid.

This power input is a continuous source for kinetic and magnetic energy and also accounts for dissipation losses as seen from the following equations showing the energy balance in the entire domain, including moving liquid, solid conducting wall, and surrounding vacuum:

$$\partial_t E_K = \dot{E}_{C_K} + \dot{E}_p + \dot{E}_{D_K} + \dot{E}_\Phi + \dot{E}_{C_M}^{KE} + \dot{E}_{M_S}^{KE}, \quad (24)$$

$$\partial_t E_M = \dot{E}_j + \dot{E}_p + \dot{E}_{C_M}^{ME} + \dot{E}_{M_S}^{ME}. \quad (25)$$

Here,  $\dot{E}_p$ ,  $\dot{E}_{C_K}$ ,  $\dot{E}_{D_K}$ ,  $\dot{E}_\Phi$ ,  $\dot{E}_{C_M}$ ,  $\dot{E}_{M_S}$ ,  $\dot{E}_j$ , and  $\dot{E}_p$  are the components of the energy balance associated with pressure, convection of kinetic energy, diffusion of kinetic energy, viscous dissipation, convection of magnetic energy, Maxwell stresses, Joule heat, and radiation (Poynting term), respectively. The mathematical definitions of these terms are

$$\begin{aligned} \dot{E}_p &= A l \nabla \cdot \left[ \left( \mathbf{u} \times \mathbf{B} - \frac{\mathbf{j}}{\sigma} \right) \times \mathbf{B} \right], & \dot{E}_p &= \nabla \cdot (\mathbf{u} p), \\ \dot{E}_{C_M}^{ME} &= (\mathbf{u} \cdot \nabla) E_M, & \dot{E}_{C_K} &= -(\mathbf{u} \cdot \nabla) E_K, \\ \dot{E}_{M_S}^{ME} &= -A l \mathbf{u} \cdot (\mathbf{B} \cdot \nabla \mathbf{B}), & \dot{E}_{D_K} &= \frac{1}{Re} \nabla^2 E_K, \\ \dot{E}_j &= -A l Re_m \frac{\mathbf{j}^2}{\sigma}, \end{aligned} \quad (26)$$

$$\begin{aligned} \dot{E}_\Phi &= -\frac{1}{Re} (\nabla \mathbf{u}) : (\nabla \mathbf{u}), \\ \dot{E}_{C_M}^{KE} &= -(\mathbf{u} \cdot \nabla) E_M, \end{aligned} \quad (27)$$

$$\dot{E}_{M_S}^{KE} = A l \mathbf{u} \cdot (\mathbf{B} \cdot \nabla \mathbf{B}).$$

It is worth noting that  $\dot{E}_{\mathcal{M}_S}^{KE}$  and  $\dot{E}_{\mathcal{M}_S}^{ME}$ , and  $\dot{E}_{C_M}^{KE}$  and  $\dot{E}_{C_M}^{ME}$  are equal with opposite signs, respectively.

Equations (24) and (25) are written in a dimensionless form using the same scales such that all energy, dissipation, and other terms can be directly compared. The physical representation of most terms in Eq. (25) are discussed in Ref. 1 and not repeated here.

The convection and pressure terms spatially integrate (over the entire domain) to zero and do not add nor remove energy from the system. At steady state, the unsteady terms are zero. The volume integral of the Poynting term can be converted into a surface integral and thus can be viewed as a source of magnetic energy to penetrate into the vacuum,  $Al \int_{\Gamma_c} [(\mathbf{u} \times \mathbf{B} - \frac{1}{\sigma} \nabla \phi) \times \mathbf{B}] \cdot \mathbf{n} d\Gamma$ . The Poynting term is zero at steady state also, with the following explanation. Consider Eq. (25) in the vacuum in proximity to a conductor. No electric currents exist, and no material is moving, so the only remaining terms are the unsteady and Poynting terms. Therefore, the Poynting term spatially integrates to zero at steady state. Thus, the only remaining non-zero terms in Eqs. (24) and (25) after spatially integrating at steady state are  $\dot{E}_{\mathcal{D}_K}$ ,  $\dot{E}_{\Phi}$ ,  $\dot{E}_{\mathcal{M}_S}$ , and  $\dot{E}_j$ . These remaining terms were plotted in Fig. 24(a). Interestingly, the Joule heat varies noticeably with changes in  $Re_m$  and reaches a local maximum at  $Re_m = 1000$ . This also means, however, that *more* energy is converted from kinetic energy to magnetic energy, through the Maxwell stress term, at  $Re_m = 1000$  compared to  $Re_m = 2000$ . Also, the steady-state integral kinetic and induced magnetic field energies were plotted together as a function of  $Re_m$  in Fig. 24(b).

The striking result from Fig. 24(b) is that the kinetic energy varies very little across a large range of  $Re_m$  (up to  $Re_m = 1000$ ). The magnetic energy grows most rapidly, and the Joule heating also increases noticeably, but for  $Re_m < 900$ , the kinetic energy of the moving liquid is always higher than that of the induced magnetic field. Based on the computations up to  $Re_m = 1000$ , the steady-state induced magnetic field energy in the fluid can be roughly estimated using the following cubic formula:

$$ME(Re_m)|_{\Omega_f} = 2.1 \times 10^{-11} Re_m^3 - 2 \times 10^{-8} Re_m^2 + 2.8 \times 10^{-5} Re_m - 5.6 \times 10^{-5}. \quad (28)$$

Using this formula, the kinetic and magnetic energies can be estimated to become equal at  $Re_m = 1320.13$ . Additional computations were carried out at  $Re_m = 1500$  and  $Re_m = 2000$ ,

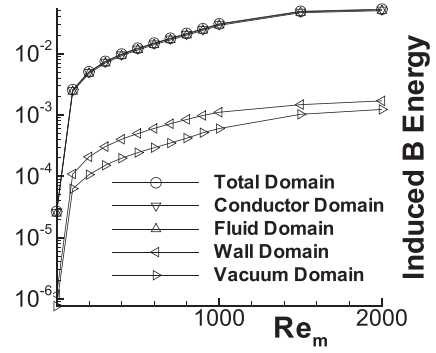


FIG. 25. The steady-state magnetic energy in different domains.

which revealed that the transition from the kinetic energy-dominated regime to the magnetic energy-dominated regime does not occur due to significant growth in the kinetic energy and a decrease in the nominal growth of the induced magnetic field energy. Besides, these additional computations resulted in non-symmetric (with respect to the  $z = 0$  plane) and unsteady flows. Due to the non-symmetric flow, both computed cases for  $Re_m = 1500$  and  $Re_m = 2000$  were computed using the full three-dimensional geometry, unlike many computed cases at lower  $Re_m$ , which utilized symmetric and anti-symmetric BCs.

Another interesting feature of the energy balance is the distribution of the magnetic energy between the conducting domain (fluid and containing walls) and the vacuum. The magnetic energy was computed in each of the domains and is plotted in Fig. 25. Interestingly, the magnetic energy in the fluid is between 1 and 2 orders of magnitude larger than that of the wall and vacuum, which are within an order of magnitude of each other, for all  $Re_m$ , and the magnetic energy seems to increase with  $Re_m$  at the same rate in all of the domains equally.

Iso-surfaces of the steady-state kinetic energy and induced magnetic field energy are plotted in Figs. 26 and 27, respectively, to analyze the energy in more detail. The velocity streamtraces (Fig. 26) show a contorted path, which changes shape with increasing  $Re_m$ . Obviously, most of the kinetic and magnetic energy is localized near the driving lid. In the liquid, the kinetic and magnetic energies resemble a “j”-shape and roughly coincide with each other at lower  $Re_m$  (Figs. 26 and 27). At higher  $Re_m$ , the “j”-shape structure of kinetic and magnetic energy breaks down.

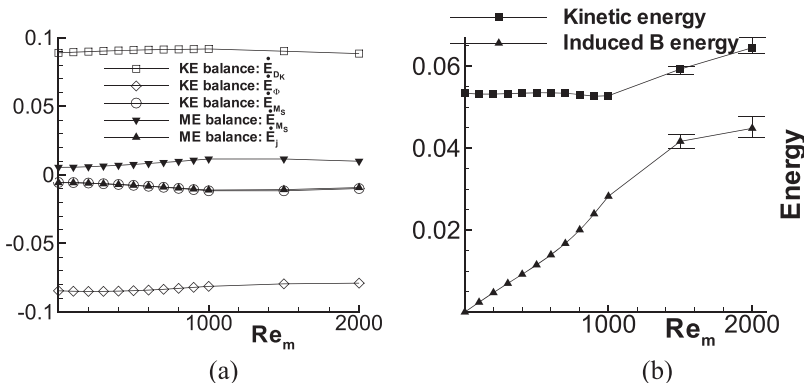


FIG. 24. Graphical representation of energy and energy components. The flows at  $Re_m = 1500$  and  $Re_m = 2000$  are unsteady. Values were computed at the last time step for points shown without variation bars. (a) Spatially integrated energy balance components in Eqs. (24) and (25). (b) The steady-state kinetic and induced magnetic field energies.

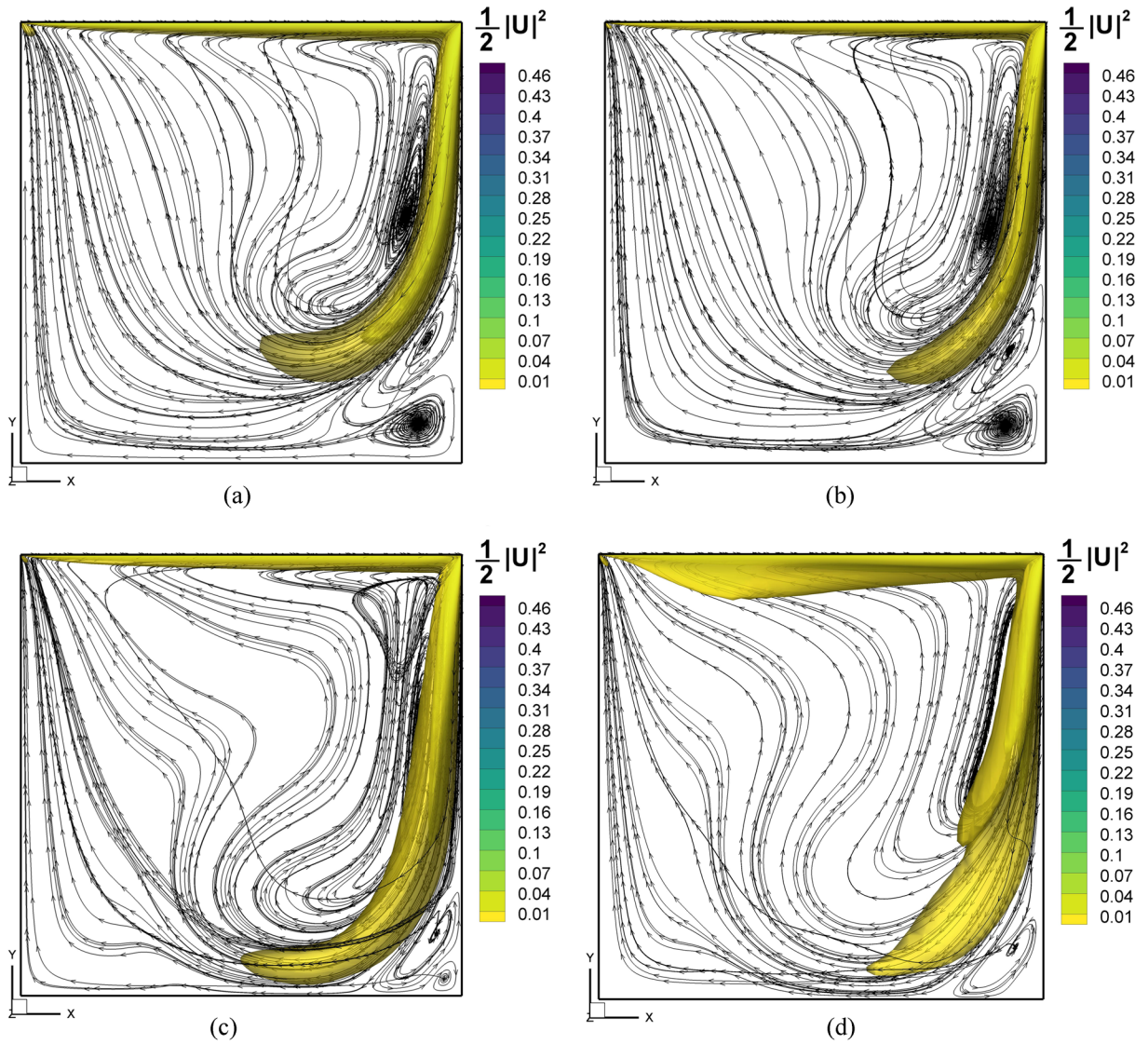


FIG. 26. Kinetic energy iso-surfaces and 3D velocity streamlines for (a)  $Re_m = 1$ , (b)  $Re_m = 100$ , (c)  $Re_m = 500$ , and (d)  $Re_m = 1000$ .

### I. Linear and non-linear dynamo tests

In this section, tests for a kinematic and full dynamo are presented. For the kinematic dynamo test, the fluid flow equations are solved first in the absence of the Lorentz force until the flow has reached a statistically steady state. Then, the velocity is fixed in time, and the induction equation is solved for the given instantaneous velocity distribution. In the dynamo theory, MHD flow is considered to be a kinematic dynamo if the induced magnetic field increases without bound. Based on the computed results in Fig. 28, the magnetic field first grows in time and then reaches a steady-state value for  $Re_m \lesssim 700$ . For all  $Re_m \gtrsim 700$ , the induced magnetic field keeps growing in time without reaching a steady state for maximal computational time of 600. For all computed cases, the maximum induced magnetic field is significantly higher than the applied one. For example, in the highest  $Re_m$  case of  $Re_m = 2000$ , the maximum induced magnetic field is more than 200 times higher than the applied one. Based on these observations, we believe that this flow has ingredients for a kinematic dynamo.

The growth rate of the induced magnetic field increases with  $Re_m$ . It is, however, difficult to precisely determine the critical magnetic Reynolds number,  $Re_{m,crit}$ , above which the flow demonstrates kinematic dynamo action because only a few cases were computed. The number of cases was limited due to a high computational cost and a need for very long computations until the magnetic field reaches the asymptotic behavior. Another limitation for  $Re_m$  values above 2000 is that the induced magnetic field penetrates further into the vacuum, requiring an even larger computational domain to permit  $\mathbf{B}^\perp = 0$  at  $\Gamma_r$ .

For the full dynamo test, the coupled MHD equations are solved until the flow reaches a statistically steady state, and then, the applied magnetic field is abruptly turned off. The MHD flow is considered to be a full dynamo if the induced magnetic field is sustained after the applied field is turned off. A full dynamo occurs when the transfer of kinetic energy, which is injected into the system via the driving lid, into magnetic energy persists when the applied field is turned off. To our knowledge, a LDC flow has never been shown to

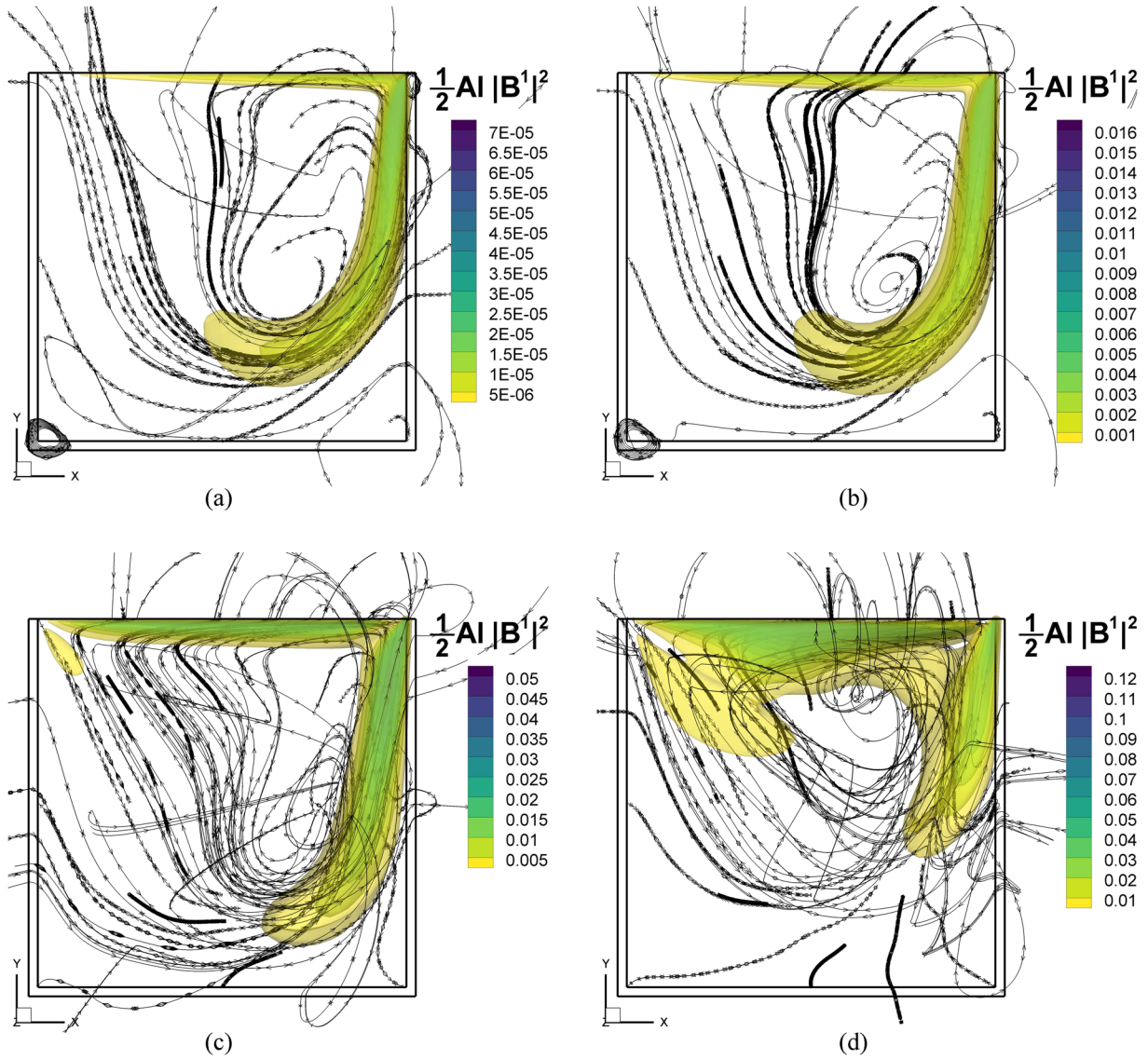


FIG. 27. Induced magnetic field energy iso-surfaces and streamtraces for (a)  $Re_m = 1$ , (b)  $Re_m = 100$ , (c)  $Re_m = 500$ , and (d)  $Re_m = 1000$ .

demonstrate, let alone tested for, dynamo physics. This test was only performed at  $Re_m = 2000$  (see Fig. 29) since these computations are very expensive. The applied magnetic field was turned off at  $t = 543.255$ . Interestingly, there is a region of

$B^1$  energy growth at around  $t = 600$ , which seems to be a turning point where the  $B^1$  energy drops below the  $B^0$  energy. The  $B^1$  energy reaches a minimum of  $E_{B^1}(\Omega_f, t = 598.5) = 0.011$

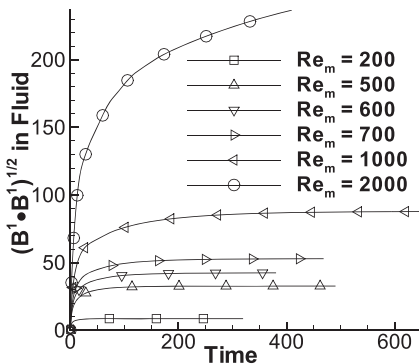


FIG. 28. Induced magnetic field energy vs. time for kinematic dynamo test.

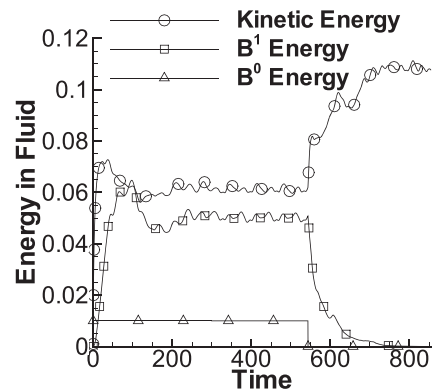


FIG. 29. Kinetic and induced magnetic field energies vs. time for the full dynamo test at  $Re_m = 2000$ .  $B^0$  was turned off at  $t = 543.255$ .

and starts to significantly increase to a local maximum of  $E_{\mathbf{B}^1}(\Omega_f, t = 607.3) = 0.0123$ , after which the  $\mathbf{B}^1$  energy continues on its nearly monotonic decent to zero.

## V. CONCLUDING REMARKS

In this study, we numerically solved the coupled fluid flow and electromagnetic equations using the full induction MHD formulation for a LDC flow of viscous, incompressible liquid subject to a strong magnetic field, which is parallel to the moving lid and perpendicular to the lid velocity vector. The primary focus in the study was on the effect of the magnetic Reynolds number on the flow inside an electrically conducting square cavity driven by a moving lid and on the magnetic field generated by the flowing liquid. To address such effects, the  $Re_m$  was changed in the computations from low values typical to the inductionless approximation ( $Re_m \ll 1$ ) to moderate and even high  $Re_m$  (up to 2000) for which dynamo-type physics might be expected, while the hydrodynamic Reynolds number and the Hartmann number were constant, at 2000 and 100, respectively. The computational domain included the electrically conducting fluid, surrounding solid walls, and an outer vacuum domain, which is sufficiently large to ensure physically correct far-field magnetic BCs. First, a new three-dimensional numerical code was developed and carefully tested using the induced magnetic field as the primary electromagnetic variable, and then, the code was applied to the LDC flow to reveal for the first time specific flow physics associated with finite  $Re_m$ , which was found to be very different from both the purely hydrodynamic flows and MHD flows at low  $Re_m$ . Many new interesting features have been observed with regard to the effect of  $Re_m$  on the MHD BL and the bulk flow, generation of a magnetic field and its penetration into vacuum, energy balance (including kinetic and magnetic field energy distributions), frozen magnetic field behavior and associated magnetic field expulsion from the fluid domain, transition to unsteady flows, and self-excitation of the magnetic field and the associated dynamo-type action at high  $Re_m$ . In addition to these interesting observations, we expect that the detailed velocity and magnetic field distributions obtained in this study for the variety of  $Re_m$  will help to establish a new database necessary for the benchmarking of existing and new full induction MHD codes, which are needed for successful advancement of several important applications such as liquid metal blankets of fusion power reactors.

A summary of changes that happen in the flow and associated flow and magnetic field features as  $Re_m$  is increased from much less than unity to the maximum value ( $Re_m = 2000$ ) employed in the present computations is the following. First of all, we have noticed a significant difference in the effect of  $Re_m$  on the flow between steady and time-dependent flows, including truly unsteady flows and those transitioning from the initial condition to a steady state. In steady-state flows, we observed that the  $Re_m$  effect on the flow is negligible for  $Re_m \lesssim 100$  as seen from the integral kinetic energy versus  $Re_m$  plotted in Fig. 24(b) and from the velocity distributions shown in Fig. 9 for several  $Re_m$  values. At the same time, the induced magnetic field in this range of  $Re_m$  changes linearly in magnitude with  $Re_m$ , but its distribution is qualitatively the same.

Moreover, the induced magnetic field is much smaller compared to the applied one in this  $Re_m$  range. These observations suggest that the inductionless approximation is still valid (at least for particular values of  $Re$  and  $Ha$  used in this study) even for  $Re_m \sim 1$  and higher,  $1 < Re_m \lesssim 100$ . This conclusion, however, is not applicable to time-dependent flows, for which the validity of the inductionless approximation seems to be limited to the conventional restriction  $Re_m \ll 1$ . Similar trends can be expected for time-periodic flows, i.e., the inductionless approximation for such time-dependent flows should be limited to  $Re_m \ll 1$ .

All computed solutions eventually converged to a steady state except for two cases at the highest  $Re_m = 1500$  and  $Re_m = 2000$ . The flow is steady for  $100 \lesssim Re_m \lesssim 1000$ , but the magnetic Reynolds number has a non-linear effect on the flow as seen from the magnetic field plot in Fig. 24(b) and Eq. (28), which approximates the integral induced magnetic field in the flow domain as a cubic polynomial of  $Re_m$ . Clearly, the inductionless approximation is not valid for  $Re_m > 100$ . The magnetic energy grows fast as  $Re_m$  is increased, while the kinetic energy almost does not significantly change. The kinetic energy and the magnetic energy were estimated to become equal at  $Re_m = 1320$  [based on Eq. (28)], based on the behavior of the induced magnetic field in the range  $0 \leq Re_m \leq 1000$ . However, additional computations revealed that the flow remains in the kinetic energy-dominated regime at  $Re_m = 1500$  and even  $Re_m = 2000$ , where a significant increase in the integral kinetic energy and a nominally lower increase in the induced magnetic field energy occur. In addition, the flow becomes unsteady and results in full three-dimensional (non-symmetric with respect to the  $z = 0$  plane) solutions. Another characteristic value is  $Re_m \approx 850$  such that for all  $Re_m$  higher than 850, the averaged magnetic field in the flow domain is higher than the applied one as seen in Fig. 8.

Magnetic Reynolds numbers higher than 100 were found to have a substantial effect on the flow structure. Both the Hartmann layers and the 2D bulk flow typical to low  $Re_m$ , or high  $Ha$ , MHD flows seem to experience significant modifications compared to the flows for which the inductionless approximation is valid. In particular, our results show that the flow is mostly two-dimensional (except for the Hartmann layers) when  $Re_m < 100$  but becomes more three-dimensional as  $Re_m$  increases. Although the analysis was limited to  $Ha = 100$ , we expect that increasing  $Ha$  would result in returning 2D features even at high  $Re_m$ , but this needs to be further studied.

A distinguished feature of the induced magnetic field is its penetration into the vacuum domain. The computations show that the behavior of the magnetic field in the insulating outer domain is similar to that of the magnetic dipole. Namely, far from the liquid domain where the magnetic field is generated, the magnetic field strength drops very fast—as one divided by the cubic distance from the conductor, in agreement with the Biot-Savart law. In doing so, about 97% of the induced magnetic energy is located in the conducting domain for all  $Re_m$ . About 4% of the energy is located in the conducting wall, and at most 3% of the energy is located in the vacuum (Fig. 25).

The observed changes in the flow and magnetic field behavior at high  $Re_m \sim 10^2$ – $10^3$  (non-linearity, unsteadiness, kinetic energy dominating over magnetic energy, and high

magnitudes of the induced magnetic field) motivated us to perform special tests to see whether or not the LDC flow can exhibit a dynamo action. Two particular numerical experiments were conducted to check for linear (kinematic) and non-linear dynamos. In the kinematic dynamo test, the full induction problem was solved for a given hydrodynamic velocity field computed in the absence of the Lorentz force. Results suggest that the MHD LDC flow may exhibit a kinematic dynamo action above a critical  $Re_m$ . In the non-linear dynamo test, the coupled MHD equations are solved until the flow reaches a statistically steady state, and then, the applied magnetic field is abruptly turned off. This test was only performed at  $Re_m = 2000$  since such computations are costly. Although no dynamo action was demonstrated, a local peak in the magnetic energy was observed, suggesting that the full dynamo might be possible at higher  $Re_m$ .

The results obtained in this study for moderate and high  $Re_m$  are also useful for implementation of approximate PV BCs as briefly discussed in Sec. II C. It is important to note that PV BCs are the true BCs for  $Re_m \ll 1$  (Ref. 17) but incompatible with the moving lid BC in the high  $Re_m$  limit. In this limit, magnetic field lines become frozen to the velocity field and, therefore, magnetic field lines become purely tangential at the driving lid. Pseudo-vacuum magnetic BCs enforce the magnetic field lines to stretch perpendicular to the boundary. The  $Re_m = 1$  case [see Fig. 27(a)] nearly matches the case of PV BCs. Contrastively, RV BCs allow non-zero tangential field components [Figs. 27(b)–27(d)]; therefore, we can expect to see significantly larger differences in the results between PV and RV BCs as  $Re_m$  is increased. Obtaining the  $Re_m$  limits for the use of the approximate PV BCs is an important practical goal as utilization of such BCs would allow much cheaper computations that do not require solving the induction equation in the outer domain. Although no full systematic studies on the comparison of different BC types were performed in the present study, our results suggest that the PV BCs should be applicable to steady-state flows for  $Re_m$  up to several hundreds until frozen magnetic field effects become pronounced. A dedicated, detailed study is needed in the future to address this issue for different flows and flow regimes, in particular, for unsteady flows, for which applicability of the PV BCs seems to be more limited compared to steady-state flows.

Regarding the use of BCs, another useful observation is the electric current distribution in the thin conducting wall. Namely, for inductionless flows, it is typical to use thin conducting wall approximation. It is most likely that the thin conducting wall approximation still holds at finite  $Re_m$  as the validity of this approximation is based on the specific current distribution associated with a small wall thickness when the current enters the wall from the liquid and then turns and flows almost tangentially through the wall. The thin-wall BCs are a geometric constraint on the system, which in our case remains unchanged regardless of  $Re_m$ .

## ACKNOWLEDGMENTS

The authors would like to thank, for their helpful discussions, Professor Jonathan Aurnou from the University of California, Los Angeles, Professor Ming-Jiu Ni from the

University of Chinese Academy of Sciences, and Professor Tomoaki Kunugi from Kyoto University. This material is based upon work supported by the U.S. Department of Energy, Office of Science, Office of Fusion Energy Sciences, under Award No. DE-FG02-86ER52123.

- <sup>1</sup>R. Moreau, *Magnetohydrodynamics* (Kluwer, 1990).
- <sup>2</sup>G. K. Batchelor, "On the spontaneous magnetic field in a conducting liquid in turbulent motion," *Proc. R. Soc. London, Ser. A* **201**, 405 (1950).
- <sup>3</sup>G. A. Glatzmaier and P. H. Roberts, "A three-dimensional convective dynamo solution with rotating and finitely conducting inner core and mantle," *Phys. Earth Planet. Inter.* **91**, 63 (1995).
- <sup>4</sup>A. Jackson, A. Sheyko, P. Marti, A. Tilgner, D. Cebren, S. Vantieghem, R. Simitev, F. Busse, X. Zhan, G. Schubert, S. Takehiro, Y. Sasaki, Y. Y. Hayashi, A. Ribeiro, C. Nore, and J. L. Guermond, "A spherical shell numerical dynamo benchmark with pseudo-vacuum magnetic boundary conditions," *Geophys. J. Int.* **196**, 712 (2013).
- <sup>5</sup>J. A. Shercliff and G. K. Batchelor, "Steady motion of conducting fluids in pipes under transverse magnetic fields," *Math. Proc. Cambridge Philos. Soc.* **49**, 136 (1953).
- <sup>6</sup>J. C. R. Hunt and G. S. S. Ludford, "Three-dimensional MHD duct flows with strong transverse magnetic fields. Part 1. Obstacles in a constant area channel," *J. Fluid Mech.* **33**, 693 (1968).
- <sup>7</sup>S. Smolentsev, N. Morley, and M. Abdou, "Code development for analysis of MHD pressure drop reduction in a liquid metal blanket using insulation technique based on a fully developed flow model," *Fusion Eng. Des.* **73**, 83 (2005).
- <sup>8</sup>A. Alemany, P. Marty, F. Plunian, and J. Soto, "Experimental investigation of dynamo effect in the secondary pumps of the fast breeder reactor Superphenix," *J. Fluid Mech.* **403**, 263 (2000).
- <sup>9</sup>S. S. Molokov, R. Moreau, and H. K. Moffatt, *Magnetohydrodynamics: Historical Evolution and Trends* (Springer Science & Business Media, 2007), Vol. 80.
- <sup>10</sup>J. D. Kotulski and M. Ulrickson, in *IEEE/NPSS 24th Symposium on Fusion Engineering* (IEEE, 2011).
- <sup>11</sup>S. Smolentsev, R. Moreau, L. Bühler, and C. Mistrangelo, "MHD thermo-fluid issues of liquid-metal blankets: phenomena and advances," *Fusion Eng. Des.* **85**, 1196 (2010).
- <sup>12</sup>N. B. Salah, A. Soulaïmani, and W. Habashi, "A finite element method for magnetohydrodynamics," *Comput. Methods Appl. Mech. Eng.* **190**, 5867 (2001).
- <sup>13</sup>G. Guj and F. Stella, "A vorticity-velocity method for the numerical solution of 3D incompressible flows," *J. Comput. Phys.* **298**, 286 (1993).
- <sup>14</sup>M. J. Pattison, K. N. Premnath, N. B. Morley, and M. A. Abdou, "Progress in lattice Boltzmann methods for magnetohydrodynamic flows relevant to fusion applications," *Fusion Eng. Des.* **83**, 557 (2008).
- <sup>15</sup>V. Shatrov, G. Mutschke, and G. Gerbeth, "Three-dimensional linear stability analysis of lid-driven magnetohydrodynamic cavity flow," *Phys. Fluids* **15**, 2141 (2003).
- <sup>16</sup>G. Rüdiger and Y. Zhang, "MHD instability in differentially-rotating cylindrical flows," *Astron. Astrophys.* **378**, 302 (2001).
- <sup>17</sup>V. Bandaru, T. Boeck, D. Krasnov, and J. Schumacher, "A hybrid finite difference-boundary element procedure for the simulation of turbulent MHD duct flow at finite magnetic Reynolds number," *J. Comput. Phys.* **304**, 320 (2016).
- <sup>18</sup>C. Gissinger, A. Iskakov, S. Fauve, and E. Dormy, "Effect of magnetic boundary conditions on the dynamo threshold of von Kármán swirling flows," *Europhys. Lett.* **82**, 29001 (2008).
- <sup>19</sup>G. Tóth, "The  $\nabla \cdot \mathbf{B} = 0$  constraint in shock-capturing magnetohydrodynamic codes," *J. Comput. Phys.* **161**, 605 (2000).
- <sup>20</sup>J. U. Brackbill and D. C. Barnes, "The effect of nonzero  $\nabla \cdot \mathbf{B}$  on the numerical solution of the magnetohydrodynamic equations," *J. Comput. Phys.* **35**, 426 (1980).
- <sup>21</sup>M.-J. Ni and M. A. Abdou, "A bridge between projection methods and SIMPLE type methods for incompressible Navier-Stokes equations," *Int. J. Numer. Methods Eng.* **72**, 1490 (2007).
- <sup>22</sup>D. Jackson John, *Classical Electrodynamics* (John Wiley & Sons, 1999).
- <sup>23</sup>M. Griebel, T. Dornseifer, and T. Neunhoffer, *Numerical Simulation in Fluid Dynamics: A Practical Introduction* (SIAM, 1997), Vol. 3.
- <sup>24</sup>A. B. Iskakov, S. Descombes, and E. Dormy, "An integro-differential formulation for magnetic induction in bounded domains: Boundary element-finite volume method," *J. Comput. Phys.* **197**, 540 (2004).

- <sup>25</sup>A. Iskakov and E. Dormy, "On magnetic boundary conditions for non-spectral dynamo simulations," *Geophys. Astrophys. Fluid Dyn.* **99**, 481 (2005).
- <sup>26</sup>J. L. Guermond, J. Léorat, and C. Nore, "A new finite element method for magneto-dynamical problems: two-dimensional results," *Eur. J. Mech: B/Fluids* **22**, 555 (2003).
- <sup>27</sup>H. Ding, C. Shu, K. S. Yeo, and D. Xu, "Numerical computation of three-dimensional incompressible viscous flows in the primitive variable form by local multiquadric differential quadrature method," *Comput. Methods Appl. Mech. Eng.* **195**, 516 (2006).
- <sup>28</sup>Y. Feldman and A. Y. Gelfgat, "Oscillatory instability of a three-dimensional lid-driven flow in a cube," *Phys. Fluids* **22**, 093602 (2010).
- <sup>29</sup>N. O. Weiss, "The expulsion of magnetic flux by eddies," *Proc. R. Soc. London, Ser. A* **293**, 310 (1966).
- <sup>30</sup>K. Messadek and R. Moreau, "An experimental investigation of MHD quasi-two-dimensional turbulent shear flows," *J. Fluid Mech.* **456**, 137 (2002).
- <sup>31</sup>R. H. Pletcher, J. C. Tannehill, and D. Anderson, *Computational Fluid Mechanics and Heat Transfer* (CRC Press, 2012).
- <sup>32</sup>J. Perot, "An analysis of the fractional step method," *J. Comput. Phys.* **108**, 51 (1993).
- <sup>33</sup>C. R. Evans and J. F. Hawley, "Simulation of magnetohydrodynamic flows—A constrained transport method," *Astrophys. J.* **332**, 659 (1988); e-print [arXiv:9809069v1](https://arxiv.org/abs/9809069v1) [[arXiv:gr-qc](https://arxiv.org/abs/9809069v1)].
- <sup>34</sup>J. Kim and P. Moin, "Application of a fractional-step method to incompressible Navier-Stokes equations," *J. Comput. Phys.* **323**, 308 (1985).
- <sup>35</sup>H. Le and P. Moin, "An improvement of fractional step methods for the incompressible Navier-Stokes equations," *J. Comput. Phys.* **92**, 369 (1991).
- <sup>36</sup>A. J. Chorin, "Numerical solution of the Navier-Stokes equations," *Math. Comput.* **22**, 745 (1968).
- <sup>37</sup>H. Araseki, "A self-correcting procedure for computational liquid metal magnetohydrodynamics," *J. Comput. Phys.* **110**, 301 (1994).
- <sup>38</sup>C. Kawczynski, S. Smolentsev, and M. Abdou, "An induction-based magnetohydrodynamic 3D code for finite magnetic Reynolds number liquid-metal flows in fusion blankets," *Fusion Eng. Des.* **109-111**, 422 (2016).
- <sup>39</sup>P. A. Davidson, *An Introduction to Magnetohydrodynamics* (AAPT, 2002).
- <sup>40</sup>B. Knaepen, S. Kassinos, and D. Carati, "Magnetohydrodynamic turbulence at moderate magnetic Reynolds number," *J. Fluid Mech.* **513**, 199 (2004).
- <sup>41</sup>I. E. Sarris, G. K. Zikos, A. P. Grecos, and N. S. Vlachos, "On the limits of validity of the low magnetic Reynolds number approximation in MHD natural-convection heat transfer," *Numer. Heat Transfer, Part B* **50**, 157 (2006).
- <sup>42</sup>J. Sommeria and R. Moreau, "Why, how, and when, MHD turbulence becomes two-dimensional," *J. Fluid Mech.* **118**, 507 (1982).
- <sup>43</sup>E. Leriche and S. Gavrillakis, "Direct numerical simulation of the flow in a lid-driven cubical cavity," *Phys. Fluids* **12**, 1363 (2000).